ELSEVIER

CrossMark

Evaluation of anisotropic constitutive models: Mixed anisotropic hardening and non-associated flow rule approach

Mohsen Safaei [a,*], Shun-lai Zang [b], Myoung-Gyu Lee [c], Wim De Waele [a]

[a] Department of Mechanical Construction and Production, Faculty of Engineering and Architecture, Ghent University, Technologiepark Zwijnaarde 903, Zwijnaarde BE9052, Belgium
[b] School of Mechanical Engineering, Xi'an Jiaotong University, No. 28, Xianning West Road, Xi'an, Shaanxi 710049, PR China
[c] Graduate Institute of Ferrous Technology (GIFT), Pohang University of Science and Technology (POSTECH), San 31, Hyoja-dong, Nam-gu, Pohang, Geongbuk 790-784, Republic of Korea

ABSTRACT

In this paper we present a non-associated plane stress anisotropic constitutive model with mixed isotropic-kinematic hardening. The quadratic Hill 1948 and non-quadratic Yld-2000-2d yield criteria [Barlat F, et al. Int J Plasticity 2003;19: 1297–1319.] are considered in the non-associated flow rule (non-AFR) model to account for anisotropic behavior. To predict accurate hardening in cyclic loading conditions, a modification of the hardening model proposed by Chun et al. [Chun BK, et al., Int J Plasticity 2002; 18: 571–595.] is adopted. This one-surface non-linear mixed isotropic-kinematic hardening model does not require loading criterion and can predict Bauschinger effect, transient behavior and permanent softening. The developed model was implemented as a user-defined material subroutine (UMAT) into the commercial finite element code ABAQUS/Standard based on fully implicit backward Euler's method. Cup drawing simulation results for an automotive sheet metal AA5754-O show that the implemented hardening model avoids under- and over-estimation of the cup height respectively generated by kinematic and isotropic hardening laws. Moreover, as will be seen in the results of highly textured AA2090-T3, both cup height and earing profile generated by non-associated flow models are in better agreement with experimental results. Finally, the Yld2004-18p and non-AFR Yld2000-2d models are compared in terms of prediction of directional Lankford coefficients and yield stresses. It is shown that a same order of accuracy that is obtained by Yld2004-18p can be achieved by the non-AFR Yld2000-2d.

© 2013 Elsevier Ltd. All rights reserved.

1. Introduction

Sheet metals generally exhibit a considerable anisotropy due to their crystallographic texture. The anisotropic mechanical characteristics of the material have a significant influence on the shape of the parts after deformation. Therefore many phenomenological models have been proposed for use in Finite Element (FE) codes to simulate the anisotropic behavior of a material. The anisotropy is mainly described on the basis of the Lankford coefficients and/or the yield stresses along the orthotropic (rolling and transverse) and diagonal axes of the metallic sheets. The different yield functions make use of different combinations of these parameters to represent a 3-dimensional surface (in case of plane stress) determining the transition between elastic and plastic deformation.

The foundation of most anisotropic yield criteria has been based on the Associated Flow Rule (AFR) hypothesis strengthened by experimental observations of Bridgman [1,2]. He performed a series of tensile tests on metals in the presence of high hydrostatic pressure and noticed that this pressure had no influence on the yielding of the material. In addition, a negligible permanent volume change was shown to exist [3]. Due to the absence of pressure sensitivity in the plastic deformation, only the deviatoric stress is involved in the formulation of the yield stress function. On the other hand, the zero plastic dilatancy (zero permanent volume change) will not be violated by using the same yield function as plastic potential (equivalency of yield function and plastic potential).

Accordingly, under the assumption of AFR, starting from Hill's quadratic anisotropy model [4], various yield functions have been proposed to describe the initial anisotropy of metallic sheets such as Barlat et al. [5–8], Banabic et al. [9], Cazacu and Barlat [10,11], Cazacu et al. [12,13], Hu [14], Bron and Besson [15], Karafillis and Boyce [16] and very recently Barlat et al. [17]. In order to accurately describe both yielding and plastic flow behavior of sheet metals, the coefficients of the above anisotropic yield functions commonly need to be optimized explicitly or iteratively

* Corresponding author. Tel.: +32 9 331 0479.
E-mail addresses: mohsen.safaei@ugent.be, msafaei@outlook.com (M. Safaei).

Nomenclature

$(\underset{\approx}{.})$	a fourth order tensor
$\tilde{\bar{\alpha}}_{1-8}$	parameters of Yld2000-2d
b	Voce isotropic hardening parameter
$\underset{\approx}{C}^e$	fourth order isotropic elasticity stiffness
C_1, C_2	kinematic hardening parameters
C	C_2/C_1
E	Young's modulus
$\bar{\varepsilon}^p$	equivalent plastic strain
ε^p	plastic strain tensor
$\bar{\varepsilon}_0^p$	parameter of Swift isotropic hardening function
$\bar{\varepsilon}^{p,1}$	equivalent plastic strain at the onset of uniaxial load reversal
ε^{el}	elastic strain tensor
ε	total strain tensor
φ	plastic strain rate direction w.r.t. rolling direction
f	yield function (associated flow rule)
f_y	yield function (non-associated flow rule)
f_p	plastic potential (non-associated flow rule)
F	yield criterion
γ	kinematic hardening parameter
H	derivative of isotropic hardening w.r.t. equivalent plastic strain
h_0, h_1 and h_2	plastic moduli
I	identity tensor
k	parameter of Swift isotropic hardening function
λ	plastic multiplier factor
λ_y, ν_y and ρ_y	parameters of Hill 1948 yield stress (Hill S-based)
λ_p, ν_p and ρ_p	parameters of Hill 1948 plastic potential function (Hill r-based)
m	first order gradient of the yield stress function
m	parameter of Yld2000-2d (6 for BCC and 8 for FCC metals)
υ	Poisson's ratio
n	parameter of Swift isotropic hardening function
n	first order gradient of the plastic potential function
q_0	equivalent plastic strain
q_1	Chaboche kinematic hardening function
q_2	Ziegler kinematic hardening function
q	total kinematic hardening function ($q = q_1 + q_2$)
q_t	total value of kinematic hardening at uniaxial tension
q_c	total value of kinematic hardening at uniaxial compression
$q_1^{(1)}$	value of Chaboche kinematic hardening at the onset of uniaxial load reversal
$q_2^{(1)}$	value of Ziegler kinematic hardening at the onset of uniaxial load reversal
Q	Voce isotropic hardening parameter
r_θ	Lankford coefficient at θ degree orientation w.r.t. rolling direction
r_b	Lankford coefficient at balanced biaxial state
σ^{trial}	trial stress tensor
σ	Cauchy stress tensor
σ_t	stress at uniaxial tension
σ_c	stress at uniaxial compression
σ_θ	initial yield stress at θ degree orientation w.r.t. rolling direction
σ_b	initial yield stress at balanced biaxial state
$\bar{\sigma}$	$\sigma - q$
σ^{iso}	isotropic hardening function
θ	loading direction w.r.t. rolling direction
$\partial(x)_y$	first derivative of x w.r.t y
$A \otimes B$	Dyadic (or tensor) product of A and B
$A : B$	double contraction of second order tensors A and B

from the experimental tensile, shear or biaxial yield stresses and Lankford coefficients.

In AFR, which is one of the cornerstones of classical plasticity theory for metals, the yield function determines both yielding and flow direction (plastic strain rate) simultaneously. However, describing a highly anisotropic material in terms of both plastic strain rate and yielding behavior with an identical function for yield and plastic potential is difficult [18]. This can, for instance, be fulfilled by using more complicated yield criteria with a large number of parameters such as the Yld2004-18p model developed by Barlat et al. [7].

From a physical point of view, experimental tension and compression tests on iron based metals and on aluminum, reported by Spitzig and Richmond [19], revealed the (linear) dependency of yield stress on the superimposed hydrostatic pressure. They also showed that an associated flow rule over-predicts the plastic dilatation in the presence of superimposed hydrostatic pressure. Therefore the AFR is unable to deal with zero plastic dilatancy and pressure sensitivity because zero plastic dilatancy requires the plastic potential to be a function of the deviatoric stress only, and must therefore be insensitive to pressure [20]. Similar observation as made by Spitzig and Richmond was reported for geologic materials by Lade et al. [21] and the invalidity of AFR for application to porous, granular, and geologic materials has been proven.

The non-associated flow rule (non-AFR) removes the artificial constraint of equality of plastic potential and yield function enforced by AFR assumption. Consequently, two separate functions for yield and plastic potential are adopted. In other words,

the yield function and plastic potential respectively describe the elastic limit and plastic strain rate direction independently. Therefore, the non-AFR could be the solution for description of simultaneous pressure sensitivity and negligible plastic dilatancy. Moreover, a larger number of experimental data can be used for calibration of each yield and plastic potential parameter resulting in a better agreement between simulation and experimental data, e.g. better prediction of yield stress and Lankford at additional orientations. Furthermore, the inability of Hill 1948 quadratic yield function for modeling the first order anomaly in balanced biaxial tension could not be because of the quadratic order of the formulation, but is rather due to the restriction forced by the equivalency of the plastic potential and yield function [22].

During the last decade, more attention has been paid on the development and implementation of non-AFR for metal plasticity. For instance, Stoughton [18] proposed a non-AFR based on Hill 1948 quadratic formulation that accurately predicted both direction-dependent Lankford coefficients and yield stresses at rolling, transverse and diagonal directions. Meanwhile, the difficulties in description of the first and second order of anomalous behavior for materials with low Lankford coefficient were resolved in this model. The reported accuracy in prediction of direction-dependent Lankford coefficients and yield stresses in the mentioned non-AFR model resulted from the sufficient degree of freedom for choosing material parameters that could match to the experimental values [20]. Continuing his previous model, Stoughton with Yoon [23] developed a pressure sensitive non-AFR model that predicted the strength differential effect observed in tension and compression tests. Cvitanic et al. [24] developed a

non-AFR based on Hill 1948 quadratic and Karafillis and Boyce non-quadratic yield functions combined with isotropic hardening which showed an improved prediction of cup heights for deep drawn cups made of an aluminum alloy. Stoughton and Yoon [25] proposed a non-AFR based anisotropic hardening model that resulted in excellent predictions of the hardening curves at 0°, 45°, 90° directions and of the balanced biaxial stress state. Improvements in prediction of cup height and springback of U-bend using non-AFR with mixed isotropic-kinematic hardening have been reported by Taherizadeh et al. [26].

In this paper, we discuss the development of non-AFR plasticity approach based on the Hill 1948 quadratic [4] and the non-quadratic Yld2000-2d [5] formulations combined with a recently proposed mixed hardening rule of Zang et al. [27]. The employed Zang's mixed hardening model improves the predictive capabilities of the well-known classical Chaboche [28] kinematic hardening by modeling the permanent softening [27]. The proposed model was implemented into the commercial FE code ABAQUS/Standard using the fully implicit backward Euler's algorithm. The multi-stage return mapping method based on the incremental deformation theory proposed by Yoon et al. [29] was used in the implemented algorithm, which enhances the convergence of the linearization algorithm significantly. Cup drawing simulation results for an automotive sheet metal AA5754-O show that the implemented non-AFR combined with the newly developed hardening model avoids under- and over-estimation of the cup height respectively generated by kinematic and isotropic hardening laws. Moreover, as will be seen in the results of highly textured AA2090-T3, both cup height and earing profile generated by non-AFR models are in better agreement with experimental results. Moreover, a comparison of the non-AFR Yld2000-2d with Yld2004-18p [7] in modeling directional Lankford coefficients and yield stresses is presented for AA2090-T3 and a fictitious material (FM8) proposed by Yoon et al. [30]. Excellent prediction of directional Lankford coefficients and yield stresses is obtained with the developed non-AFR Yld2000-2d for both considered materials.

2. Constitutive model

In the following sections, the italic bold letters represent second-order tensors such as σ, and the fourth order tensors are shown by underscript double tilde such as $\underset{\approx}{C}^e$.

2.1. Hardening model

It is well known that upon load reversal the Bauschinger effect, transient behavior and some degree of stress shift (permanent softening) can be observed. In addition, for mild steel sheets, the abnormal evolution of the hardening curve (stagnation behavior) may be observed [31]. One of the most commonly used mixed isotropic-kinematic hardening models was proposed by Armstrong and Frederick [32] and Chaboche [28]. This model can predict Bauschinger effect and the evanescent strain memory effect (transient behavior) observed in cyclic loadings by adding a relaxation term (recall term) to Ziegler's [33] linear kinematic hardening model. This model is defined by

$$d\boldsymbol{q} = C\frac{(\boldsymbol{\sigma}-\boldsymbol{q})}{f}d\bar{\varepsilon}^p - \gamma\boldsymbol{q}d\bar{\varepsilon}^p \qquad (1)$$

where C and γ are hardening parameters and f denotes the yield function in associated flow plasticity. Second order tensors $\boldsymbol{\sigma}$ and $\boldsymbol{q}$ respectively denote the Cauchy stress and kinematic hardening function. For sake of brevity, we agree that $\bar{\boldsymbol{\sigma}} = \boldsymbol{\sigma}-\boldsymbol{q}$.

Chaboche [28] proposed superposing multiple terms of Eq. (1) as one model such that

$$\boldsymbol{q} = \boldsymbol{q}_1 + \boldsymbol{q}_2 + \boldsymbol{q}_3 + \cdots + \boldsymbol{q}_N \qquad (2)$$

where N is the number of back-stress terms.

The prediction of permanent softening has been included in several multi-surface models such as Geng and Wagoner [34], Yoshida and Uemori [35] and Lee et al. [36]. To capture the Bauschinger effect, transient behavior and permanent softening in the framework of a one-surface cyclic model, Chun et al. [37] proposed a modification to the isotopic part of mixed isotropic-kinematic hardening with a two-term Chaboche model. In his model, the second Chaboche term is described by a Ziegler's linear kinematic hardening. This second term turns into zero in case of load reversal, thus a loading criterion is required in the model.

A loading criterion for a general plane-stress case can be formulated using the stress tensors at the previous and current time steps. For example, the state of the loading at the current step is defined as reversal if the angle between these two stress tensors is between 90° and 270° [38]. Nonetheless, Zang et al. [27] described that this loading criterion must be carefully formulated otherwise an incorrect stress might be obtained.

Recently, inspired by the work of Chun et al. [37], Zang et al. [27] proposed a one-surface cyclic hardening that predicts Bauschinger effect, transient behavior and permanent softening. Analogously to the Chaboche model, his model generates the saturating hardening after several cycles (see Fig. 1). In Zang's model, the isotropic hardening function is described in the following form:

$$\sigma^{iso}(\bar{\varepsilon}^p) = \sigma_0 + Q(1-e^{-b\bar{\varepsilon}^p}) - C_1/\gamma(1-e^{-\gamma\bar{\varepsilon}^p}) \qquad (3)$$

It is noticed that the first and second terms in the right side of Eq. (3) constitute the Voce isotropic hardening law, and the third term is the integrated form of the one-term Chachoche kinematic hardening model in uniaxial loading condition.

The kinematic hardening function consists of a two-term Chaboche model in which the first term is a non-linear Armstrong and Frederick and the second term is Ziegler's linear kinematic hardening:

$$d\boldsymbol{q} = d\boldsymbol{q}_1 + d\boldsymbol{q}_2 \qquad (4a)$$

$$d\boldsymbol{q}_1 = C_1\frac{\bar{\sigma}}{f}d\bar{\varepsilon}^p - \gamma\boldsymbol{q}_1 d\bar{\varepsilon}^p \qquad (4b)$$

$$d\boldsymbol{q}_2 = C_2\frac{\bar{\sigma}}{f}d\bar{\varepsilon}^p \qquad (4c)$$

where C_1, C_2 and γ are material parameters. The non-linear term $\boldsymbol{q}_1$ in Eq. (4b) is solely associated to the transient behavior and
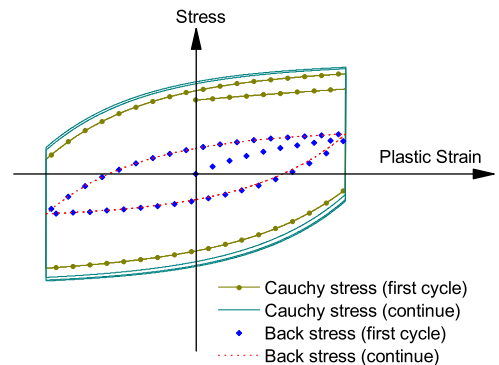

Fig. 1. An example of cyclic loading generated by Zang mixed hardening model. The saturating behavior is properly generated at high cycles.

improves its prediction. The second term, Ziegler's linear kinematic hardening law in Eq. (4c), was used to generate a constant stress offset. It must be noted that considering Zang's mixed hardening model, the introduction of the modified isotropic hardening law Eq. (3) improves the capability of the constitutive model in modeling of transient behavior since it causes the back-stress $\bar{\varepsilon}^{p,1}$ to be only associated to the transient behavior [27].

For uniaxial loading, Zang's model can be integrated to

$$\sigma_t = \sigma^{iso} + q_t$$
$$= \sigma_0 + Q(1 - e^{-b\bar{\varepsilon}^p}) + c_2\bar{\varepsilon}^p \tag{5}$$

where σ_t and q_t respectively denote Cauchy stress and back-stress in uniaxial tension. For uniaxial compression due to change of stress direction we have

$$\sigma_c = -\sigma^{iso} + q_c \tag{6}$$

σ_c and q_c being respectively Cauchy stress and back-stress during reversed loading. In general, the integrated form of the $\boldsymbol{q}_1$ tensor (q_1) during uniaxial and reversed loading can be written as

$$q_1 = \omega C_1/\gamma + \left(q_1^{(1)} - \omega c_1/\gamma\right) e^{-\omega\,\gamma(\bar{\varepsilon}^p - \bar{\varepsilon}^{p,1})} \tag{7}$$

where $\omega = \pm 1$ gives the flow direction (i.e., +1 and −1 respectively denote forward and reversed loading) and $q_1^{(1)}$ and $\bar{\varepsilon}^{p,1}$ respectively denote the value of q_1 and accumulated plastic strain at the onset of load reversal [39]. Similarly, for second term of kinematic hardening we write

$$q_2 = \omega C_2(\bar{\varepsilon}^p - \bar{\varepsilon}^{p,1}) + q_2^{(1)} \tag{8}$$

with $q_2^{(1)}$ being the values of q_2 at the onset of load reversal. Considering the load reversal ($\omega = -1$), the combination of Eqs. (7) and (8) gives the total kinematic hardening denoted by q_c

$$q_c = -C_1/\gamma + \left(q_1^{(1)} + C_1/\gamma\right) e^{\gamma(\bar{\varepsilon}^p - \bar{\varepsilon}^{p,1})} - C_2(\bar{\varepsilon}^p - \bar{\varepsilon}^{p,1}) + q_2^{(1)} \tag{9}$$

In this paper, the Swift [40] isotropic hardening law is also used for some of the performed simulations. The Swift isotropic hardening is defined by

$$\sigma = k(\bar{\varepsilon}_0^p + \bar{\varepsilon}^p)^n \tag{10a}$$

$$\bar{\varepsilon}_0^p = \left(\frac{\sigma}{k}\right)^{1/n} \tag{10b}$$

with k, $\bar{\varepsilon}_0^p$ and n being the material parameters.

It must be mentioned that Zang's mixed isotropic-kinematic hardening model is considered for the stress-update integration scheme. In the next section the non-AFR is combined with this hardening model.

2.2. Anisotropic yield functions

In AFR, the yield function (f_y) determines the occurrence of plastic deformation and rate of plastic strain, simultaneously. The function which is directly involved in determination of rate of plastic strain is referred to as plastic potential (f_p), which is identical to yield stress function in AFR assumption.

In case of AFR Hill 1948 two formulations exist, the parameters of either of which can be calibrated using directional plastic strain ratios (referred to as Hill r-based) or directional yield stresses (referred to as Hill S-based). Parameters of either of those variations can be calibrated using either an optimization approach or explicit function of directional yield stresses or Lankford coefficients.

The Hill r-based model requires Lankford coefficients (r-values) at rolling direction (RD), diagonal direction (DD) and transverse direction (TD), respectively denoted by r_0, r_{45} and r_{90}. The parameters of Hill S-based model are calibrated using yield stresses at

the mentioned orientations denoted by $\sigma_0, \sigma_{45}, \sigma_{90}$ as well as that of balanced biaxial state σ_b.

The Hill S-based yield function denoted by f_{Hill-S} is defined as

$$f_{Hill-S} = (\bar{\sigma}_{11}^2 + \lambda_y\bar{\sigma}_{22}^2 - 2\nu_y\bar{\sigma}_{11}\bar{\sigma}_{22} + 2\rho_y\bar{\sigma}_{12}^2)^{1/2} \tag{11}$$

where λ_y, ν_y and ρ_y are yield function parameters.

The Hill r-based denoted by f_{Hill-r} is described as

$$f_{Hill-r} = (\bar{\sigma}_{11}^2 + \lambda_p\bar{\sigma}_{22}^2 - 2\nu_p\bar{\sigma}_{11}\bar{\sigma}_{22} + 2\rho_p\bar{\sigma}_{12}^2)^{1/2} \tag{12}$$

where λ_p, ν_p and ρ_p are material parameters.

The non-quadratic Yld2000-2d yield function proposed by Barlat et al. [5] is also evaluated in this work. This function is based on a linear transformation of two functions (φ' and φ'') of deviatoric stress tensors. The Yld2000-2d yield function is defined by

$$f = \left[\frac{1}{2}(\varphi' + \varphi'')\right]^{1/m} \tag{13}$$

where

$$\varphi' = (X_1' - X_2')^m, \quad \varphi'' = (2X_2'' + X_1'')^m + (2X_1'' + X_2'')^m \tag{14}$$

The coefficient m, which is associated to crystallographic structure, is 6 for BCC and 8 for FCC type metals. $X_{1,2}'$ and $X_{1,2}''$ are the principal values of the linear transformation on the stress deviator $\tilde{\boldsymbol{s}}'$ and $\tilde{\boldsymbol{s}}''$ respectively.

$$\tilde{\boldsymbol{s}}' = L'.\boldsymbol{\sigma}, \tilde{\boldsymbol{s}}'' = L''.\boldsymbol{\sigma} \tag{15}$$

and

$$\begin{bmatrix} L_{11}' \\ L_{12}' \\ L_{21}' \\ L_{22}' \\ L_{66}' \end{bmatrix} = \begin{bmatrix} 2/3 & 0 & 0 \\ -1/3 & 0 & 0 \\ 0 & -1/3 & 0 \\ 0 & 2/3 & 0 \\ 0 & 0 & 1 \end{bmatrix} \begin{bmatrix} \alpha_1 \\ \alpha_2 \\ \alpha_7 \end{bmatrix}, \begin{bmatrix} L_{11}'' \\ L_{12}'' \\ L_{21}'' \\ L_{22}'' \\ L_{66}'' \end{bmatrix}$$

$$= \frac{1}{9}\begin{bmatrix} -2 & 2 & 8 & -2 & 0 \\ 1 & -4 & -4 & 4 & 0 \\ 4 & -4 & -4 & 1 & 0 \\ -2 & 8 & 2 & -2 & 0 \\ 0 & 0 & 1 & 0 & 9 \end{bmatrix} \begin{bmatrix} \alpha_3 \\ \alpha_4 \\ \alpha_5 \\ \alpha_6 \\ \alpha_8 \end{bmatrix} \tag{16}$$

Eight experimental data such as yield and Lankford coefficients ($r_0, r_{45}, r_{90}, r_b, \sigma_0, \sigma_{45}, \sigma_{90}, \sigma_b$) are required to determine the α_{1-8} coefficients.

2.3. Non-associated flow model

In non-AFR, the two independent formulations of yield stress and plastic flow direction respectively determine the yielding and direction of plastic strain rate. The yield function f_y is addressed by Eqs. (11) and (13) respectively for non-AFR Hill 1948 and non-AFR Yld2000-2d. However, for non-AFR Yld2000-2d the parameters of yield function are optimized solely based on directional yield stresses at every 15° from RD ($\sigma_0, \sigma_{15}, \sigma_{30}, \sigma_{45}, \sigma_{60}, \sigma_{75}, \sigma_{90}$) as well as that of balanced biaxial stress (σ_b).

In non-AFR the yield criterion F is

$$F = f_y(\bar{\boldsymbol{\sigma}}) - \sigma^{iso}(\bar{\varepsilon}^p) \tag{17}$$

The plastic flow direction ($\boldsymbol{n}$) is determined by the plastic potential (f_p) described in Eqs. (12) and (13) in case of non-AFR Hill 1948 and non-AFR Yld2000-2d respectively. The plastic potential of non-AFR Yld2000-2d follows the same formulation of Yld2000-2d as defined in Eq. (13). However, it requires Lankford coefficients for unidirectional loading in different orientations ($r_0, r_{15}, r_{30}, r_{45}, r_{60}, r_{75}, r_{90}$) as well as that of balanced biaxial loading (r_b) for parameters optimization.

The non-associated plastic flow rule is described by

$$d\boldsymbol{\varepsilon^p} = d\lambda\boldsymbol{n} \tag{18}$$

where

$$\boldsymbol{n} = \partial f_p/\partial\overline{\boldsymbol{\sigma}} \tag{19}$$

$d\lambda$ is the plastic multiplier factor (compliance) to be determined by using loading-unloading criterion, and the second order tensor $\boldsymbol{n}$ is the plastic flow direction. It is noticed that due to the use of plastic potential f_p instead of yield stress function f_y, the normality hypothesis is no longer valid in non-AFR.

The concept of non-AFR and AFR for AA2090-T3 is shown in Fig. 2.

The principle of plastic work equivalence is described by

$$f_y(\overline{\boldsymbol{\sigma}})d\overline{\varepsilon}^p = \overline{\boldsymbol{\sigma}} : d\boldsymbol{\varepsilon^p} \tag{20}$$

Applying Euler's theory for any first order homogenous function of f

$$\overline{\boldsymbol{\sigma}} : \frac{\partial f(\overline{\boldsymbol{\sigma}})}{\partial\overline{\boldsymbol{\sigma}}} = f(\overline{\boldsymbol{\sigma}}) \tag{21}$$

Therefore, applying Euler's theory for continuously differentiable yield function and plastic potential we write

$$\overline{\boldsymbol{\sigma}} : \boldsymbol{n} = f_p \tag{22a}$$

$$\overline{\boldsymbol{\sigma}} : \boldsymbol{m} = f_y \tag{22b}$$

where the second order tensor $\boldsymbol{m}$ is the normal to the yield surface

$$\boldsymbol{m} = \partial f_y/\partial\overline{\boldsymbol{\sigma}} \tag{23}$$

Substituting Eq. (18) into Eq. (20) and then applying Eq. (22a)

$$d\overline{\varepsilon}^p = \frac{\overline{\boldsymbol{\sigma}} : d\boldsymbol{\varepsilon^p}}{f_y(\overline{\boldsymbol{\sigma}})} = d\lambda\frac{\overline{\boldsymbol{\sigma}} : \partial f_p/\partial\overline{\boldsymbol{\sigma}}}{f_y(\overline{\boldsymbol{\sigma}})} = d\lambda\frac{f_p(\overline{\boldsymbol{\sigma}})}{f_y(\overline{\boldsymbol{\sigma}})} \tag{24}$$

This definition ($d\overline{\varepsilon}^p = d\lambda f_p/f_y$) was used by Cvitanic et al. [24] for the case of isotropic hardening. However, for linearization and stress-update algorithm in case of complex mixed hardenings this leads to a very laborious numerical description in which the rate of change of effective plastic strain ($\dot{\overline{\varepsilon}}^p$) will be a complex function of rate of change of compliance factor ($\dot{\lambda}$). Therefore an alternative with $f_p/f_y = 1$ in Eq. (24) can save computational cost and development effort so that

$$d\overline{\varepsilon}^p = d\lambda \tag{25}$$

It must be noted that this simplification does not lead back to AFR. This is due to the fact that the normal to the plastic potential (and not yield function) always has been considered for plastic strain rate direction. This simplification has been adopted by

Stoughton [18], Stoughton and Yoon [20,22,25], Taherizadeh et al. [26]. Similarly, for sake of simplification, the description defined in Eq. (25), is accepted in the remainder of this paper.

3. Numerical integration algorithm

The implicit integration algorithm begins with evaluating whether the current step is in elastic or in plastic domain. An elastic process implies that the stress state is inside the yield surface and thus $F < 0$ and $d\lambda = 0$. Conversely, if the stress state of the material is nested on the yield surface ($F = 0$) then besides the yield criterion, a complimentary postulate is required for determination of loading/unloading state of the deformation process. By additional plastic deformation (loading condition) the plastic compliance factor $d\lambda$ will be non-zero and moreover the stress state of material will remain on the yield surface ($F = 0$ and $\dot{f}_y > 0$). On the other hand, the stress state can still be on the yield surface ($F = 0$) without plastic deformation occurring such that $d\lambda = 0$. In this case that can be called pure elastic or elastic unloading, the rate of change of yield stress surface will be equal or less than zero, $\dot{f}_y \leq 0$. The case where $\dot{f}_y = 0$ is referred to as neutral loading. The described loading/unloading condition can be found in the form of Kuhn–Tucker complementary condition [41]:

$$d\lambda \geq 0, \quad F \leq 0 \text{ and } d\lambda F = 0 \tag{26}$$

It is seen that the consistency condition that simply restricts the stress state inside or on the yield surface and to which we shall return later is already included in the Kuhn–Tucker condition. For sake of brevity and notational convenience, we consider equivalent plastic strain and back-stress tensors as internal variables. Accordingly, we rewrite the increments of equivalent plastic strain $\Delta\overline{\varepsilon}^p$ and back-stress functions in Eqs. (4b) and (4c) as follows:

$$\Delta q_0 = \Delta\overline{\varepsilon}^p = \Delta\lambda h_0 \tag{27a}$$

$$\Delta\boldsymbol{q}_1 = \Delta\lambda\boldsymbol{h}_1 \tag{27b}$$

$$\Delta\boldsymbol{q}_2 = \Delta\lambda\boldsymbol{h}_2 \tag{27c}$$

where h_0, $\boldsymbol{h}_1$ and $\boldsymbol{h}_1$ are plastic moduli [41].

$$h_0 = 1 \tag{28a}$$

$$\boldsymbol{h}_1 = C_1\overline{\boldsymbol{\sigma}}/f_p - \gamma\boldsymbol{q}_1 \tag{28b}$$

$$\boldsymbol{h}_2 = C_2\overline{\boldsymbol{\sigma}}/f_p \tag{28c}$$

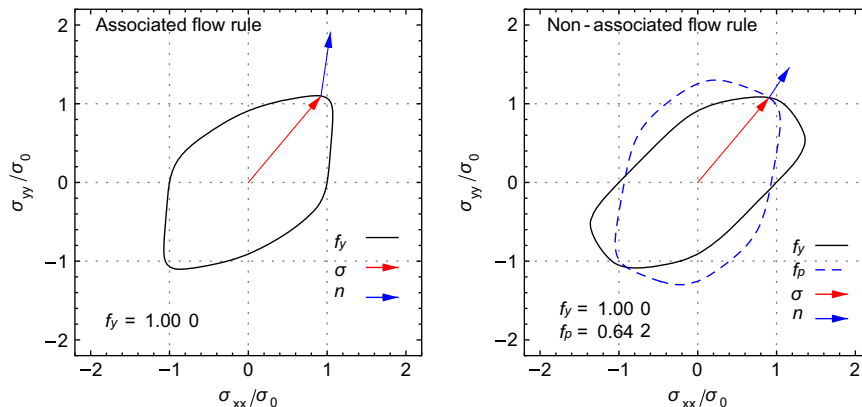**Fig. 2.** Concept of associated (left) and non-associated (right) flow rule (f_y=yield function; f_p=plastic potential; $\boldsymbol{\sigma}$=Cauchy stress; $\boldsymbol{n}$=plastic strain rate direction). These data are based on non-AFR Yld2000-2d for AA2090-T3 at $\text{ArcTan}(\sigma_{yy}/\sigma_{xx})=50°$.

Therefore the consistency condition for Eq. (17) is written as

$$dF = df_y(\boldsymbol{\sigma} - \boldsymbol{q}_1 - \boldsymbol{q}_2) - d\sigma^{iso}(q_0) = 0 \tag{29}$$

Additive decomposition of strain increments into elastic and plastic components gives

$$\Delta\boldsymbol{\varepsilon} = \Delta\boldsymbol{\varepsilon}^{el} + \Delta\boldsymbol{\varepsilon}^{p} \tag{30}$$

where $\Delta\boldsymbol{\varepsilon}^{el}, \Delta\boldsymbol{\varepsilon}^{p}$ and $\Delta\boldsymbol{\varepsilon}$ are respectively increments of elastic, plastic and total strain tensors.

The Hookean elasticity for hypoelastic materials gives

$$\Delta\boldsymbol{\sigma} = \underset{\approx}{C}^e : \Delta\boldsymbol{\varepsilon}^{el} \tag{31}$$

where the symmetric fourth order tensor $\underset{\approx}{C}^e$ describes the isotropic elasticity of the materials. Substituting the additive decomposition of strain increments in Eq. (30) into the Hookean elasticity equation (31) gives

$$\Delta\boldsymbol{\sigma} = \underset{\approx}{C}^e : (\Delta\boldsymbol{\varepsilon} - \Delta\boldsymbol{\varepsilon}^{p}) \tag{32}$$

Substituting Eq. (27a) into Eq. (27c) and into the consistency condition (29) and using Hooke's law (32) and also using the non-associated flow rule in Eq. (18) after some manipulation leads to

$$\Delta\lambda = \frac{\partial F_\sigma : \underset{\approx}{C}^e : \Delta\boldsymbol{\varepsilon}}{-\partial F_q h + \partial F_\sigma : \underset{\approx}{C}^e : \boldsymbol{n}}$$

$$= \frac{\boldsymbol{m} : \underset{\approx}{C}^e : \Delta\boldsymbol{\varepsilon}}{\boldsymbol{m} : \underset{\approx}{C}^e : \boldsymbol{n} + \boldsymbol{m} : (\boldsymbol{h}_1 + \boldsymbol{h}_2) + H} \tag{33}$$

where

$$H = \partial F_{q0} \tag{34}$$

As described before, the second order tensors of $\boldsymbol{n}$ and $\boldsymbol{m}$ respectively denote plastic flow direction and normal to the yield surface. The scalar H describes the tangent of isotropic hardening function with respect to equivalent plastic strain q_0.

Different integration schemes have been proposed to solve the rate constitutive equations for a given set of initial conditions. For instance Wilkins [42] suggested the first radial return scheme for J_2 plasticity. The fully implicit return mapping algorithm, which is adopted in this paper, gained considerable popularity due to its unconditional stability and moreover the quadratic convergence rate that is the inherent characteristic of the Newton–Raphson iteration method employed in this technique.

As we use the fully implicit Backward Euler's integration scheme, the increments in the plastic strain and all internal variables q_0, $\boldsymbol{q}_1$ and $\boldsymbol{q}_2$ are calculated at the end of step $(n+1)$ and the yield condition is enforced at the end of the step [43]. Thus the integration scheme for the non-associated model is written as

$$\boldsymbol{\varepsilon}_{(n+1)} = \boldsymbol{\varepsilon}_{(n)} + \Delta\boldsymbol{\varepsilon} \tag{35a}$$

$$\boldsymbol{\varepsilon}^{p}_{(n+1)} = \boldsymbol{\varepsilon}^{p}_{(n)} + \Delta\lambda_{(n+1)}\boldsymbol{n}_{(n+1)} \tag{35b}$$

$$q_{0,(n+1)} = q_{0,(n)} + \Delta\lambda_{(n+1)} \tag{35c}$$

$$\boldsymbol{q}_{1,(n+1)} = \boldsymbol{q}_{1,(n)} + \Delta\lambda_{(n+1)}\boldsymbol{h}_{1,(n+1)} \tag{35d}$$

$$\boldsymbol{q}_{2,(n+1)} = \boldsymbol{q}_{2,(n)} + \Delta\lambda_{(n+1)}\boldsymbol{h}_{2,(n+1)} \tag{35e}$$

$$\boldsymbol{\sigma}_{(n+1)} = \underset{\approx}{C}^e : (\boldsymbol{\varepsilon}_{n+1} - \boldsymbol{\varepsilon}^{p}_{(n+1)}) \tag{35f}$$

$$F_{n+1}(\boldsymbol{\sigma}_{(n+1)}, q_{i,(n+1)}) = 0 \tag{35g}$$

It is noticed that the described integration scheme is implicit in terms of plasticity parameter $\Delta\lambda_{(n+1)}$, flow direction $\boldsymbol{n}_{(n+1)}$ and plastic moduli $\boldsymbol{h}_1$ and $\boldsymbol{h}_2$.

The plastic strain increment $\Delta\boldsymbol{\varepsilon}^{p}_{(n+1)}$ at the end of the time increment $\Delta t_{(n+1)} = t_{(n+1)} - t_{(n)}$ is given by

$$\Delta\boldsymbol{\varepsilon}^{p}_{(n+1)} = \boldsymbol{\varepsilon}^{p}_{(n+1)} - \boldsymbol{\varepsilon}^{p}_{(n)} \tag{36}$$

By substituting Eq. (36) into the integrated form of Eq. (32) gives

$$\Delta\boldsymbol{\sigma} = -\underset{\approx}{C}^e \Delta\boldsymbol{\varepsilon}^{p}_{(n+1)} \tag{37}$$

and

$$\boldsymbol{\sigma}_{(n+1)} = \boldsymbol{\sigma}^{trial} - \underset{\approx}{C}^e : \Delta\boldsymbol{\varepsilon}^{p}_{(n+1)} \tag{38}$$

where $\boldsymbol{\sigma}^{\text{trial}}$ and $\Delta\boldsymbol{\sigma} = -\underset{\approx}{C}^e : \Delta\boldsymbol{\varepsilon}^{p}$ respectively denote the trial stress of elastic predictor step and plastic corrector. During the elastic predictor step the stress is explicitly updated using the total strain. Subsequently at the plastic corrector or so called relaxation step, the stress is returned to the yield surface at time increment $t_{(n+1)}$ using the Newton–Raphson method based on the linearization of a set of equations Eqs. (35a)–(35g) [44]. This linearization is carried out with respect to the plastic strain $\Delta\boldsymbol{\varepsilon}^{p}_{(n+1)}$ assuming the total strain is constant. Using Newton–Raphson for linearization of any equation such as $g(\Delta\lambda) = 0$ at the k-th iteration we write

$$g^{(k)} + \left(\frac{dg}{d\Delta\lambda}\right)^{(k)} \delta\lambda^{(k)} = 0 \tag{39}$$

where

$$\Delta\lambda^{(k+1)} = \Delta\lambda^{(k)} + \delta\lambda^{(k)} \tag{40}$$

$\delta\lambda^{(k)}$ being the iterative change in the $\Delta\lambda$ at the k-th iteration.

Therefore the update expressions in Eqs. (35a)–(35g) can be cast in the following forms suitable for the Newton–Raphson iteration scheme:

$$\boldsymbol{\varepsilon}^{p(k+1)} = \boldsymbol{\varepsilon}^{p(k)} + \Delta\boldsymbol{\varepsilon}^{p(k)} = \boldsymbol{\varepsilon}^{p(k)} - \underset{\approx}{C}^{e-1} : \Delta\boldsymbol{\sigma}^k \tag{41a}$$

$$q_0^{(k+1)} = q_0^{(k)} + \Delta q_0^{(k)} \tag{41b}$$

$$\boldsymbol{q}_1^{(k+1)} = \boldsymbol{q}_1^{(k)} + \Delta\boldsymbol{q}_1^{(k)} \tag{41c}$$

$$\boldsymbol{q}_2^{(k+1)} = \boldsymbol{q}_2^{(k)} + \Delta\boldsymbol{q}_2^{(k)} \tag{41d}$$

$$\Delta\lambda^{(k+1)} = \Delta\lambda^{(k)} + \delta\lambda^{(k)} \tag{41e}$$

$$\boldsymbol{\sigma}^{(k+1)} = \boldsymbol{\sigma}^{(k)} + \Delta\boldsymbol{\sigma}^{(k)} \tag{41f}$$

At the end of the k-th iteration the $\Delta\boldsymbol{\sigma}^{(k)}$, $\Delta q_0^{(k)}$, $\Delta\boldsymbol{q}_1^{(k)}$ and $\Delta\boldsymbol{q}_2^{(k)}$ are determined and their corresponding accumulated values are updated and sent for the next iteration. The iteration continues until the convergence to the updated yield surface is obtained within an acceptably small tolerance. Subsequently, the constitutive solutions are passed into FE. The detailed fully implicit integration scheme is described in Appendix A.

For the plane stress conditions such as when shell elements are used, the elastic and plastic strains for the through thickness direction are explicitly determined at the end of the converged step:

$$\varepsilon^{p}_{33,(n+1)} = \varepsilon^{p}_{33,(n)} - \Delta\varepsilon^{p}_{11} - \Delta\varepsilon^{p}_{22} \tag{42a}$$

$$\varepsilon^{el}_{33,(n+1)} = \varepsilon^{el}_{33,(n)} - v(\Delta\varepsilon^{el}_{11} + \Delta\varepsilon^{el}_{22})/(1-v) \tag{42b}$$

It is worth noting that the convergence of the Newton–Raphson method inherently is faded at large strains and the initial guess has a considerable influence on the convergence of the iteration scheme i.e., the quadratic convergence rate is achieved only if the approximation of initial value is within the radius of convergence. Therefore to obtain the convergence at larger strains, the multi-stage return mapping method based on the incremental

deformation theory proposed by Yoon et al. [29] has been applied in the implementation of return mapping algorithm.

4. Prediction of 1-D stress–strain response

AA2090-T3 and AA5754-O aluminum alloys have been selected for the evaluation of non-AFR anisotropic functions and hardening, respectively. In addition to the AA2090-T3, a fictitious material (FM8) proposed by Yoon et al. [30] is considered for evaluation of non-AFR Yld2000-2d. This material exhibits a considerable aniso-tropic behavior in a sense that two maxima are observed in the Lankford coefficients between rolling direction (RD) and trans-verse direction (TD). The other considered material, the highly textured AA2090-T3 aluminum alloy shows severe anisotropic behavior for instance it has a planar anisotropy equal to −1.125. Moreover, as depicted in Fig. 18, the experimental circular cup drawing of this material shows 6 ears. On the other hand, the alloy AA5454-O is used in automobile structural members and shows considerable stress shift (permanent softening) upon load reversal. Its mechanical behavior, i.e. normalized yield stresses (normalized with respect to rolling direction) as well as Lankford coefficients at different orientations, show a lesser level of anisotropy (planar anisotropy of 0.065) compared with those of highly textured AA2090-T3.

According to Yoon et al. [30,45], there is a straight relation between profile and number of peaks of Lankford coefficients distribution between 0° and 90° with number and profile of ears in a deep drawn cup. Furthermore, they described the connection between directional yield stresses distribution with earing profile. This is why accurate prediction of directional Lankford coefficients and yield stresses by the employed anisotropic constitutive model is essential. In this paper we show that using non-AFR Yld2000-2d the predicted Lankford coefficients and normalized yield stresses are in excellent agreement with input data for FM8 and experi-mental data for AA2090-T3.

In must be mentioned that the isotropic elasticity is assumed for all studied materials with Young's modulus $E = 70$ GPa and Poisson's ratio $\nu = 0.33$. The isotropic hardening of FM8 is chosen to be similar to that of AA2090-T3.

4.1. Prediction of flow stress

For AA5454-O, uniaxial tension/compression (T/C) experimen-tal results at RD and different pre-strains (0.025, 0.05 and 0.078) are available from Lee et al. [46]. The T/C stress versus plastic strain curve was implemented as UMAT in Abaqus using different hardening models: (i) isotropic hardening according to Swift in Eq. (10), (ii) two-term kinematic hardening of classical Chaboche in Eq. (4) and finally (iii) Zang's model in Eqs. (3) and (4). The hardening parameters are presented in Table 1.

Comparison of predicted and experimental T/C curves is plotted in Fig. 3. It is seen that the kinematic and isotropic hardening model result respectively in under- and over-estimation of the stress upon load reversal. The overestimation of the hardening by using isotropic hardening is simply due to missing the Bauschinger effect. As seen in Fig. 3 the under- and overestimation due to respectively kinematic and isotropic hardening is increased at higher pre-strains. It is also noticed that the permanent softening effect is more pronounced at higher pre-strains. As opposed to the isotropic and kinematic hardening models, application of Zang's mixed hardening model leads to stress versus plastic strain curves that are very close to the experimental ones. It must be noted that all the simulations for AA5754-O material are based on non-AFR Hill 1948. The effect of hardening models on the cup drawing simulations of AA5754-O is presented in the next section.

Table 1
Hardening parameters.

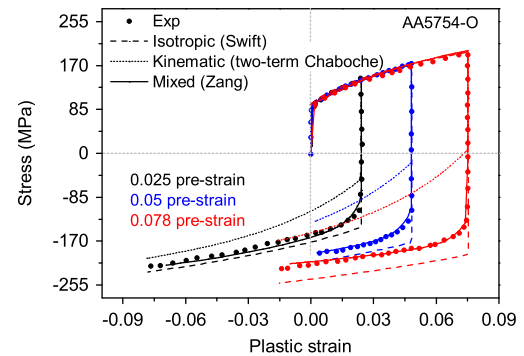| Parameter | Unit | AA5754-O | | | AA2090-T3& FM8 |
		Isotropic (Swift)	Kinematic (two-term Chaboche)	Mixed hardening (Zang)	Isotropic (Swift)
σ_0	MPa	94.8	94.8	94.8	279.6
k	MPa	452.6	–	–	646
n	–	0.34	–	–	0.227
$\bar{\varepsilon}_0^p$	–	0.01	–	–	0.025
Q	MPa	–	–	126.4	–
b	–	–	–	16.1	–
C_1	MPa	–	1997.3	4665.3	–
γ	–	–	23	212	–
C_2	MPa	–	409.6	204.8	–

Fig. 3. Comparison of experimental and simulated T/C hardening curves at different pre-strains for AA5754-O using various hardening models and non-AFR Hill 1948 anisotropic model.

Table 2
Experimental/input yield stresses ratios.

Material	0°	15°	30°	45°	60°	75°	90°	b
AA2090-T3 (Exp.)	1.000	0.961	0.910	0.811	0.810	0.882	0.910	1.035
AA5754-O (Exp.)	1.000	–	–	0.923	–	–	0.938	0.996
FM 8 (Input)	1.000	1.020	1.045	1.050	1.045	1.020	1.000	1.000

Table 3
Experimental/input Lankford (r-value) coefficients.

Material	0°	15°	30°	45°	60°	75°	90°	b
AA2090-T3 (Exp.)	0.212	0.327	0.692	1.577	1.039	0.538	0.692	0.670
AA5754-O (Exp.)	0.760	–	–	0.710	–	–	0.790	–
FM8 (Input)	0.6	1	0.75	0.3	0.75	1	0.6	1

Table 4
Hill 1948 anisotropic parameters.

Material	ν_p	ρ_p	λ_p	ν_y	ρ_y	λ_y
AA2090-T3	0.175	2.238	0.427	0.637	2.571	1.207
AA5754-O	0.432	1.349	0.978	0.556	1.576	0.975
FM8	0.375	1	1	0.5	1.314	1

4.2. Prediction of anisotropy

The experimental normalized yield stresses and Lankford coefficients at different orientations for AA5754-O, AA2090-T3

Table 5
Yld2000-2d anisotropic parameters.

Model	α_1	α_2	α_3	α_4	α_5	α_6	α_7	α_8	m
AA2090-T3									
Potential (f_p)	−0.856	1.154	−0.293	0.326	0.683	0.482	0.752	1.024	8
Yield (f_y)	−0.713	2.037	1.629	0.69	0.552	−1.057	1.255	1.263	8
AFR	0.488	1.377	0.754	1.025	1.036	0.904	1.231	1.485	8
FM8									
Potential (f_p)	2.946	−2.946	0.399	1.421	−1.421	-0.399	1.213	−1.822	8
Yield (f_y)	0.814	1.002	2.129	0.571	−0.34	1.224	0.975	−1.123	8
AFR	0.958	0.958	0.968	1.016	1.016	0.968	0.863	1.012	8

Fig. 4. Normalized tensile yield stress distribution for FM8.

Fig. 5. Lankford coefficient distribution for FM8.
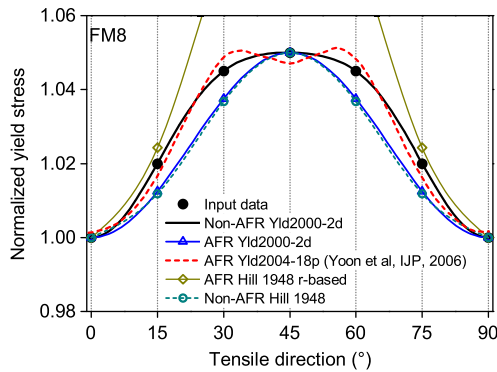
Fig. 6. Normalized tensile yield stress distribution for AA2090-T3.

and FM8 are presented in Tables 2 and 3. The corresponding Hill 1948 yield stress and plastic potential anisotropic parameters are shown in Table 4. The anisotropic parameters of non-AFR Hill 1948 for AA5754-O are used for simulation of cup drawing in the next section. The mechanical properties of AA2090-T3 can be found in Chung et al. [47] and Yoon et al. [48]. For AA2090-T3 and FM8, the experimental/input $r_0, r_{45}, r_{90}, r_b, \sigma_0, \sigma_{45}, \sigma_{90}$ and σ_b were used for optimization of AFR based Yld2000-2d parameters. However, the experimental/input $r_0, r_{15}, r_{30}, r_{45}, r_{60}, r_{75}, r_{90}, r_b$ and $\sigma_0, \sigma_{15}, \sigma_{30}, \sigma_{45}, \sigma_{60}, \sigma_{75}, \sigma_{90}, \sigma_b$ respectively were used to optimize parameters of Yld2000-2d plastic potential and yield function. The Yld2000-2d anisotropic parameters are provided in Table 5. The parameter optimization was performed using a Levenberg–Marquardt inverse approach.

To compare the predictive capabilities of different anisotropic models presented in this paper, directional normalized yield stresses and Lankford coefficients for FM8 and AA2090-T3 were simulated. Figs. 4 and 6 show the simulated normalized yield stresses for FM8 and AA2090-T3, respectively. And, Figs. 5 and 7 present the simulated Lankford coefficients for FM8 and AA2090-T3, respectively.

The directional Lankford and normalized yield stress predictions made by Yld2004-18p are reported in Yoon et al. [30]. In Figs. 4 and 6 we see that the predictive capability of yield stresses by the non-AFR Yld2000-2d is dominant over other models. Moreover, non-AFR Hill 1948 and AFR Yld-2000-2d are only accurate at 0°, 45°, 90°. In the same figure, a weak prediction of yield stress is observed for AFR Hill 1948 r-based.

In Figs. 5 and 7, the directional Lankford coefficients of respectively FM8 and AA2090-T3 are presented for the studied models. In Fig. 5 it is seen that non-AFR Yld2000-2d excellently predicts the input Lankford coefficients of FM8. In Fig. 7 for AA2090-T3 it is shown that the peak and trough (low point) respectively at 45° and 75° are accurately predicted by the Yld2004-18p and non-AFR Yld2000-2d. As will be shown in the next section, accurate prediction of these peaks and troughs
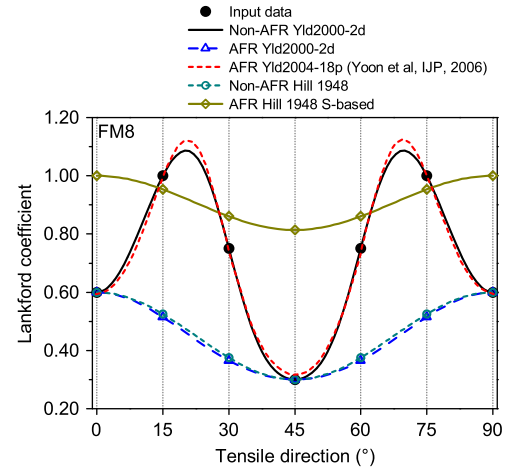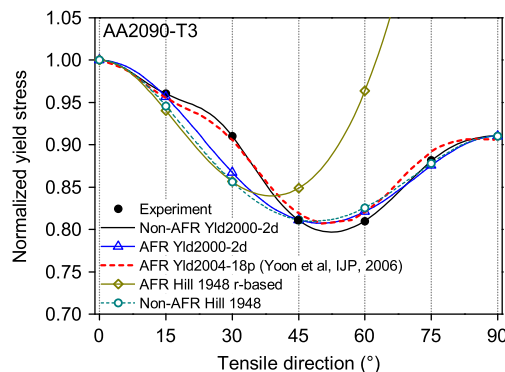
results in accurate prediction of number and height of the ears in the deep drawn cup. In Fig. 7 it is also noticed that the AFR Yld2000-2d and non-AFR Hill 1948 are accurate in predicting Lankford coefficients at 0°, 45°, 90°. However, comparing AFR Yld2000-2d with non-AFR Hill 1948 at other orientations shows that the results of AFR Yld2000-2d are closer to the experimental results. Moreover, AFR Hill 1948 S-based is not accurate in modeling the Lankford coefficients.

Two-dimensional representation of AFR and non-AFR of studied anisotropic models is presented in Figs. 8 and 10 respectively for AA2090-T3 and FM8. Moreover, the three-dimensional representation of AFR Yld2000-2d and non-AFR Yld2000-2d components (plastic potential and yield function) for AA2090-T3 and FM8 respectively is shown in Figs. 9 and 11. From these plots, it can be concluded that a higher degree of complexity can be modeled by the non-AFR formulation compared with AFR models.
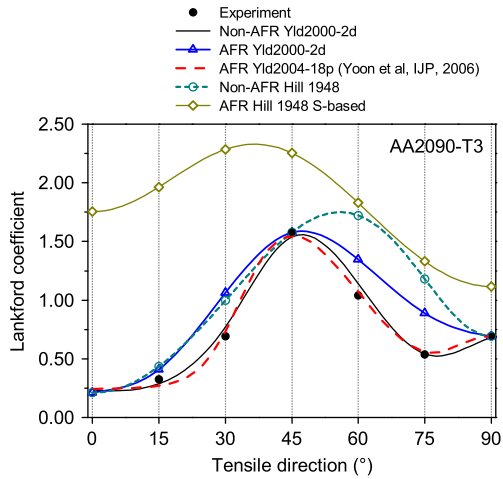
Fig. 7. Lankford coefficient distribution for AA2090-T3.

According to the non-associated flow rule (18) and (19) the outward normal to the plastic potential determines the plastic strain rate direction and consequently the corresponding Lankford coefficient. The outward normal direction to the yield function (considering the AFR model) and plastic potential (considering the non-AFR) is schematized in Fig. 12. At an in-plane loading direction of θ with regard to the RD the plastic strain rate direction makes an angle of φ with the RD. The variation of φ with respect to θ for AA2090-T3 and FM8 respectively is shown in Figs. 13 and 14. It is seen that, in general, the Mises and AFR and non-AFR Hill 1948 models present a simple variation of plastic strain rate direction with respect to RD. Conversely, for both considered materials the AFR and non-AFR Yld2000-2d can predict more detailed variation by their formulations.

5. Application to cup drawing simulation

The results of cup drawing simulations for AA2090-T3 and AA5754-O are presented. For AA2090-T3, different anisotropic
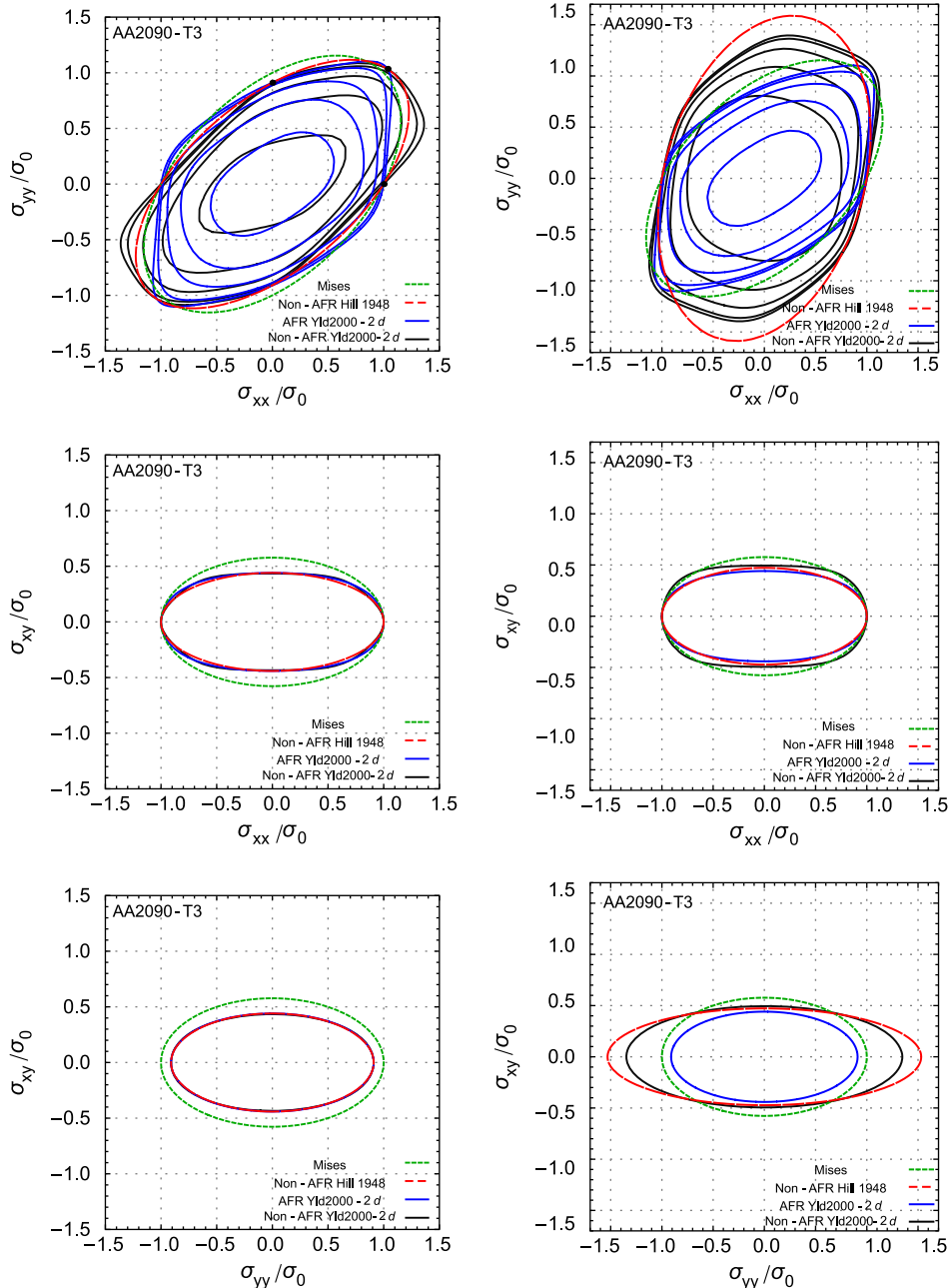
Fig. 8. Two-dimensional representation of various yield stress (left column) and plastic potential (right column) surfaces for AA2090-T3.

Material : AA2090−T3
AFR Yld2000−2d

Non−AFR Yld2000−2d (yield stress function)   **Non−AFR Yld2000−2d (plastic potential function)**
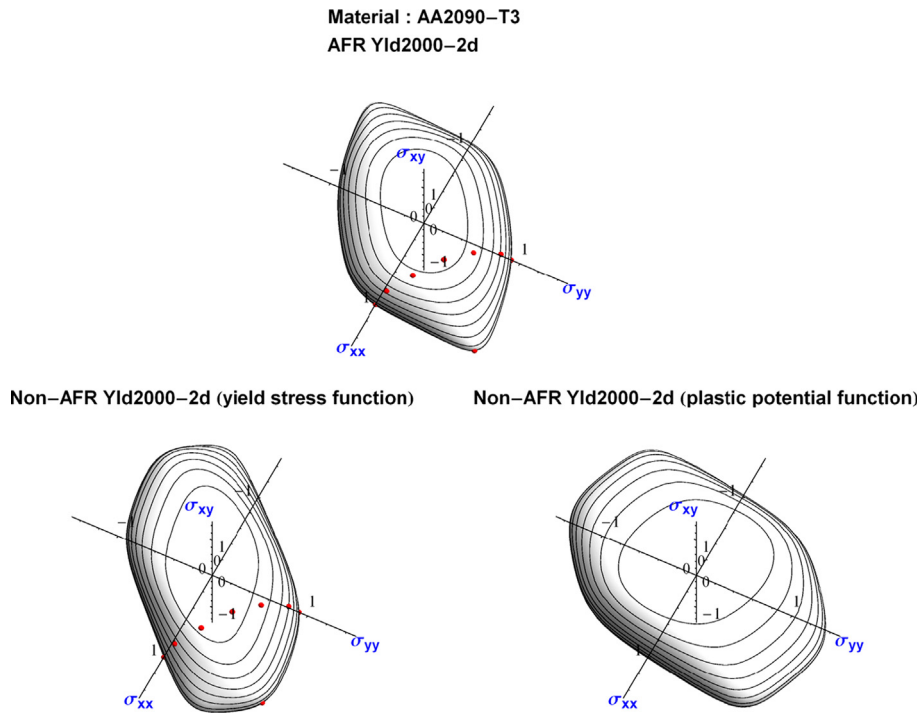
Fig. 9. Three-dimensional representation of AFR Yld2000-2d and non-AFR one (plastic potential and yield function) for AA2090-T3. Small circles denote experimental yield points at seven uniaxial directions and one balanced biaxial state.
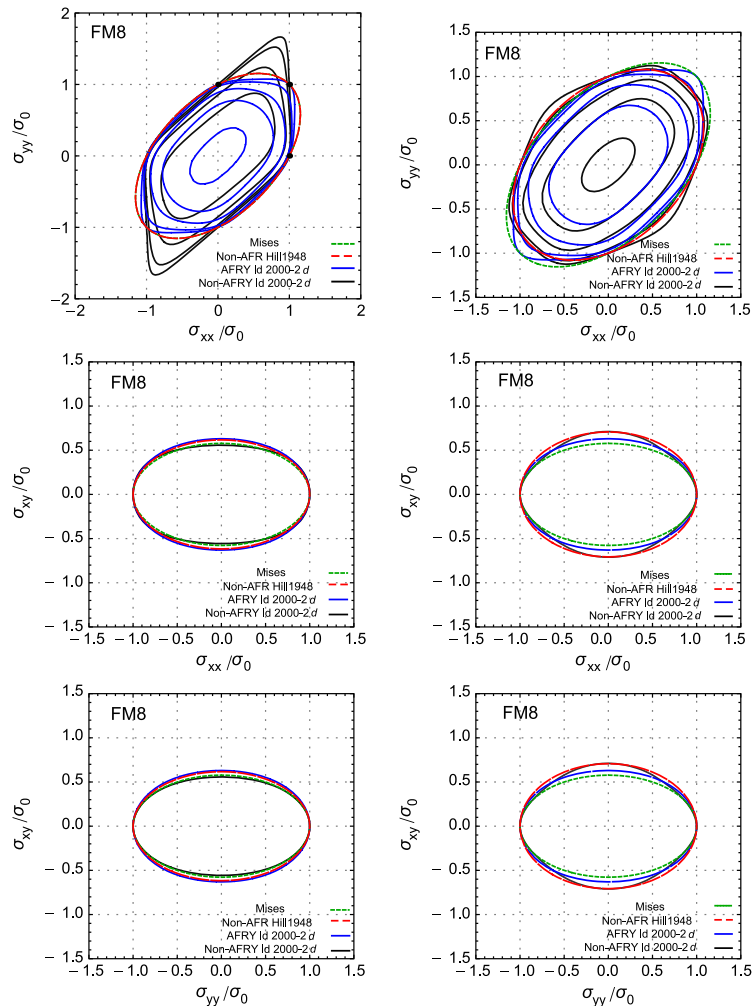
Fig. 10. Two-dimensional representation of various yield (left column) and plastic potential surfaces (right column) for FM8.
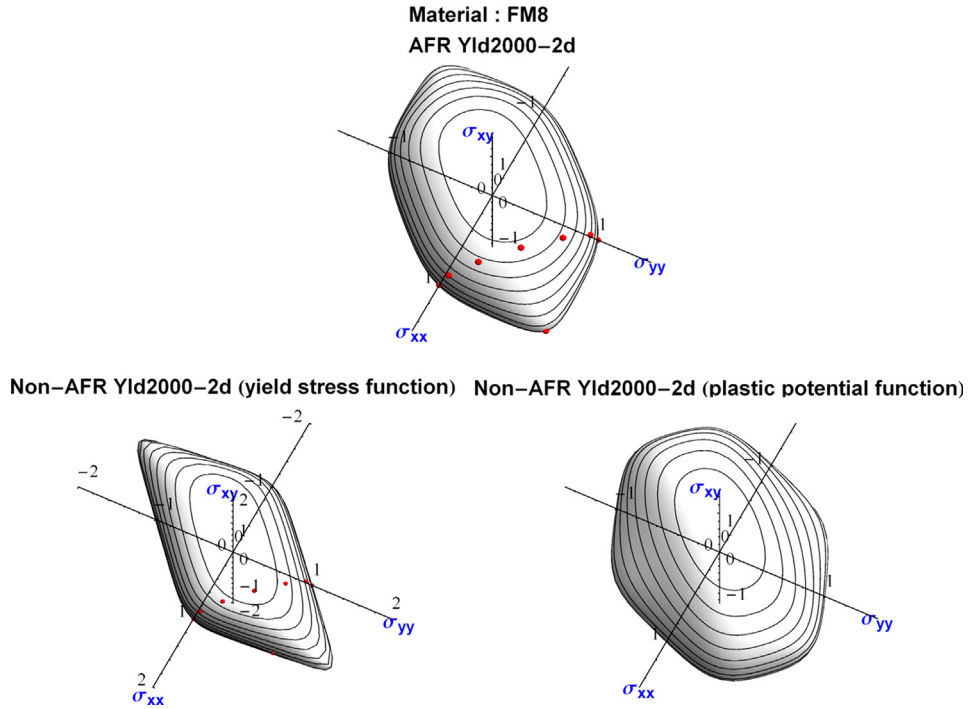
Fig. 11. Three-dimensional representation of AFR Yld2000-2d and non-AFR one (plastic potential and yield function) for FM8. Small circles denote experimental yield points at seven uniaxial directions and one balanced biaxial state.
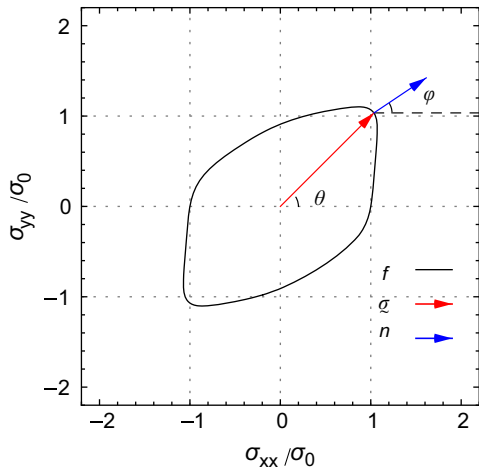
Fig. 12. Schematic of plastic strain rate orientation (φ) at an in-plane loading direction of θ with regard to the RD.

Fig. 14. Angular orientation of plastic strain rate vector φ at various loading directions θ with respect to RD obtained by various AFR and non-AFR models for FM8.

Fig. 13. Angular orientation of plastic strain rate vector φ at various loading directions θ with respect to RD obtained by AFR and non-AFR models for AA2090-T3.
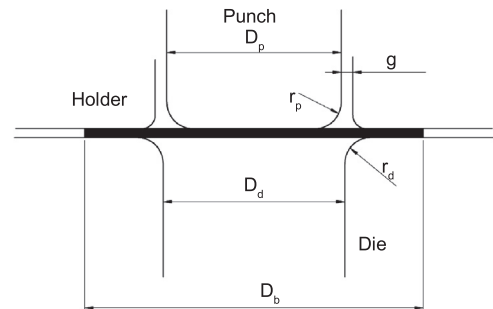
Fig. 15. Tool geometry for cylindrical cup drawing.

models (AFR and non-AFR Hill 1948 and Yld2000-2d) were studied and results were compared with the experimentally determined cup profiles. Regarding the AA5754-O, nonetheless, the cup drawing simulations are based on non-AFR Hill 1948 with different hardening models where no experimental cup drawing result is available. However, as discussed later, those data are

Table 6
Tool dimensions (unit: mm).

D_p	D_d	D_b	r_p	r_d	G
97.46	101.48	158.76	12.7	12.7	2.7
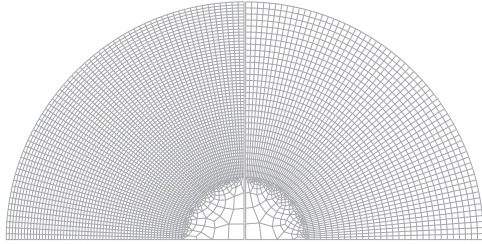
Fig. 16. Initial mesh for AA2090-T3 (left) and AA5754-O (right).
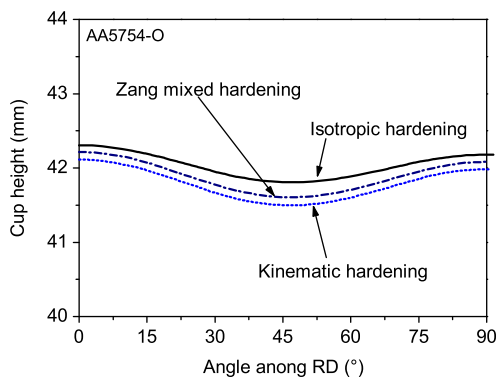
Fig. 17. Cup height simulation using non-AFR Hill 1948 and three hardening models.

Fig. 18. Cup height prediction for AA2090-T3 using AFR and non-AFR Hill 1948.

Fig. 19. Cup height prediction for AA2090-T3 using AFR Yld2000-2d and non-AFR Yld2000-2d and Hill 1948.

interesting in a sense that they lead to similar conclusions as observed in reported simulations of U-bend test [36].

The cup drawing process is schematized in Fig. 15 and the tool dimensions are given in Table 6. Due to orthogonal symmetry observed in the specimens, only one quarter of the sheet was modeled. The blanks of AA5754-O and AA2090-T3 are modeled using respectively 2147 and 3800 first order reduced integration quadrilateral shell elements respectively with 10 and 15 Gauss integration points. Initial mesh is shown in Fig. 16. The reason for different number of elements was using two different computational sources for the simulations.

A blank holder force of 5.5 kN for the quarter model (corresponding to approximately 1% of the initial yield stress) was considered in the simulations. This force was found to be high enough to avoid wrinkling in the rim area. A coulomb friction coefficient equal to 0.1 was assumed.

Three hardening models were evaluated for cup height prediction of AA5754-O. As before, the hardening models are (i) isotropic hardening according to Swift in Eq. (10), (ii) two-term kinematic hardening of classical Chaboche in Eq. (4) and finally (iii) Zang's mixed hardening model in Eqs. (3) and (4). The cup height predictions using the non-AFR Hill 1948 with anisotropy parameters in Table 4 and hardening parameters in Table 1 are plotted in Fig. 17. As noticed in the same figure, the same over- and underestimation of the stress–strain curve respectively obtained by isotropic and kinematic hardening (Fig. 3) is observed in the cup profile. However, due to more realistic prediction of T/C behavior, Zang's mixed hardening model avoids the under- and overestimation obtained by the two other hardening models. Interestingly, the same trend is observed for the U-bend springback test for an
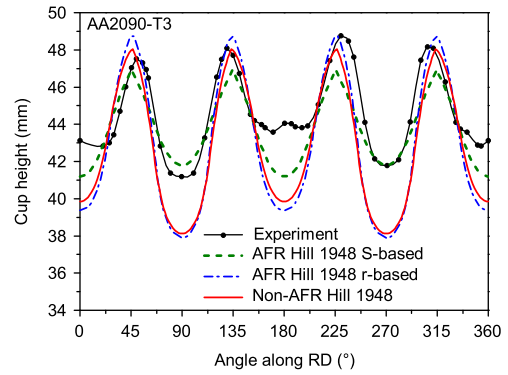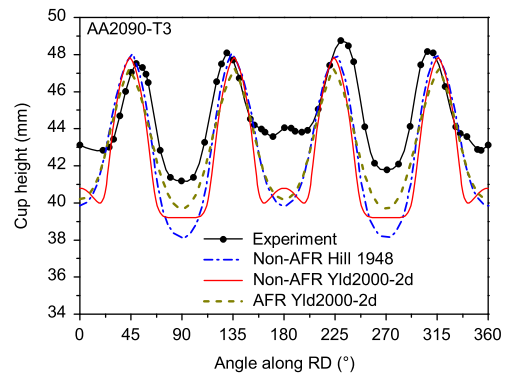
identical material using isotropic, kinematic and an accurate two-surface hardening model [36].

Fig. 18 shows simulated and experimental cup profiles of AA2090-T3 using AFR and non-AFR Hill 1948. The experimental cup profile exhibits four big ears located at 45°, 135°, 225° and 315° and two small ears at 0° (360°) and 180°. However, none of the Hill 1948 presented variations could predict more than four ears. That is due to the quadratic order of the yield and potential functions. The predicted troughs for all three Hill 1948 models are weak. On the other hand, respectively Hill's non-AFR based and r-based models predict a cup height closer to the experimental ones.

In Fig. 19, cup height profiles predicted by AFR and non-AFR Yld2000-2d are presented. For sake of comparison, the non-AFR Hill 1948 is also plotted in the same figure. Among these models, only non-AFR Yld2000-2d predicts the small ears at 0° (360°) and 180° in addition to the big ears presenting the correct number of ears in accordance with experimental results. Similar cup heights at large peaks are predicted by non-AFR Yld2000-2d and non-AFR Hill 1948. Similar to Hill 1948 S-based in Fig. 18, the AFR Yld2000-2d underestimates the cup height at the main 4 peaks. However, the same model predicts the troughs closer to the experimental ones when compared with non-AFR Hill 1948 and non-AFR Yld2000-2d. Fig. 20 presents final cup shape, Mises stresses and effective plastic strains for AA2090-T3 using non-AFR Hill 1948 and AFR and non-AFR Yld2000-2d. It is observed that the non-AFR Yld2000-2d predicts a higher level of complexity in the earing profile, i.e. a sharp transition from trough to peak. Furthermore, the higher equivalent plastic strain (SDV18 in right column) predicted by the non-AFR Yld2000-2d can be interpreted as a higher degree of plastic deformation compared to other models. Consequently, higher Mises equivalent stress is simulated by non-AFR 2000-2d.
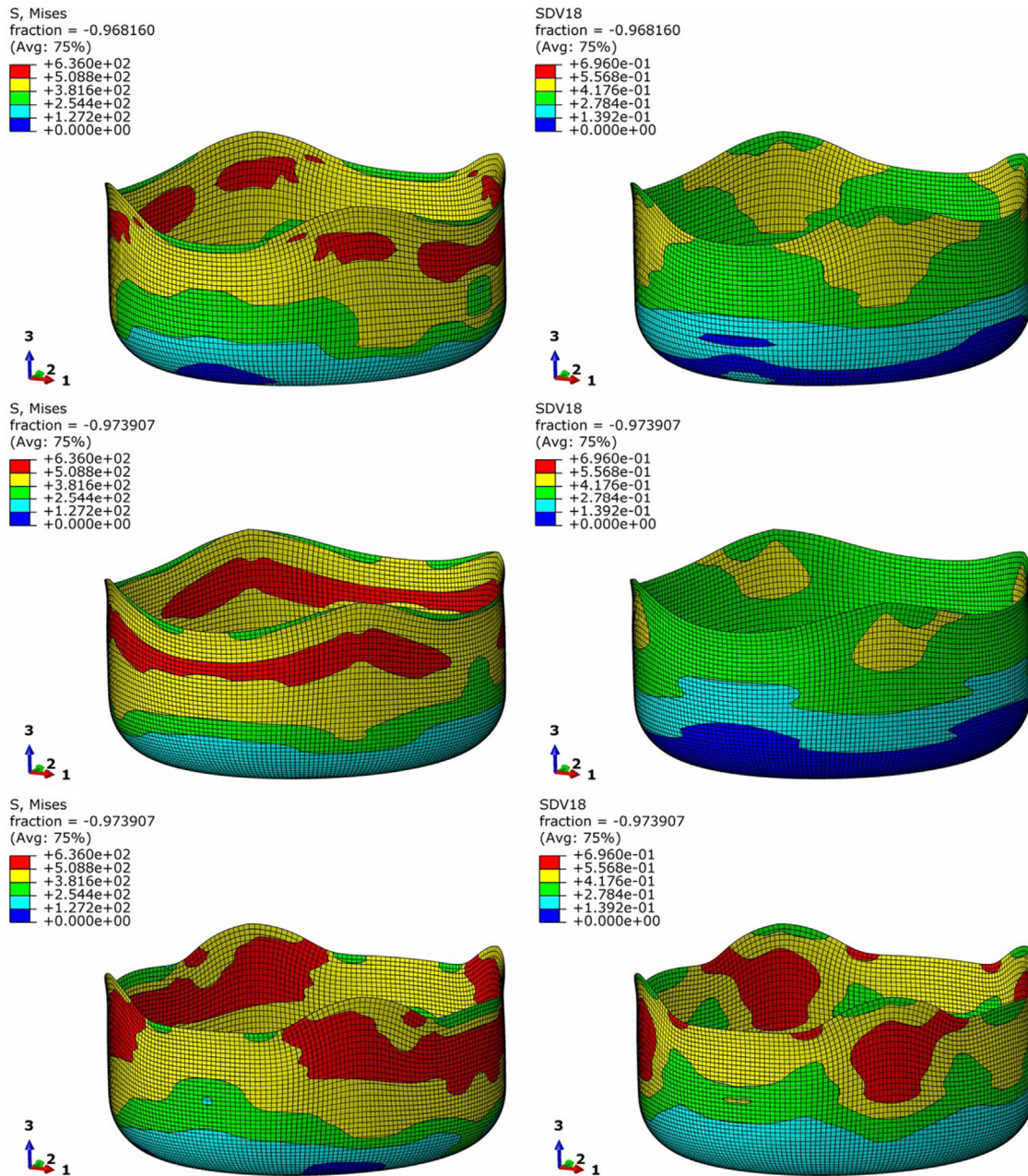
Fig. 20. Final cup shape and distribution of Mises stress (left) and equivalent plastic strain (right). From top to bottom respectively, non-AFR Hill 1948, AFR Yld2000-2d and non-AFR Yld2000-2d.

6. Summary

We developed associated and non-associated flow rules of Hill 1948 and Yld2000-2d combined with a mixed hardening of Zang et al. [27]. The AFR and non-AFR based Hill 1948 and Yld2000-2d as well as Yld2004-18p were compared with uniaxial yield stresses and Lankford coefficients at different orientations for a highly textured AA2090-T3 aluminum alloy and FM8. An excellent accuracy in prediction of directional yield stresses and Lankford coefficients was achieved by the non-AFR Yld2000-2d. It is shown that a same order of accuracy that is obtained by the Yld2004-18p can be achieved by non-AFR Yld2000-2d. Moreover, cup drawing simulations were performed based on presented models for AA5754-O and AA2090-T3 aluminum alloys. The cup deep drawing simulations for AA5754-O using isotropic, kinematic and mixed hardening were carried out. The results show that the over- and underestimation of the hardening curve respectively generated by isotropic and kinematic hardening models is directly reflected in the predicted cup height. For AA2090-T3, the predicted cup height from isotropic hardening and non-AFR Yld2000-2d shows a considerable improvement compared with that of AFR Yld2000-2d as well as other presented models. It was shown that only non-AFR Yld2000-2d can predict the exact number of 6 ears as observed in experimental results. Finally, a slight improvement compared to AFR Hill 1948 was observed by using its non-AFR counterpart.

Acknowledgments

Appendix A. linearization of the constitutive model

The update expressions in Eqs. (35a)–(35g) can be written in the following forms suitable for the Newton–Raphson iterative scheme:

$$a = -\varepsilon^p + \varepsilon^p_{(n)} + \Delta\lambda n = 0$$
$$b_0 = -q_0 + q_{0,(n)} + \Delta\lambda h_0 = 0$$
$$b_1 = -q_1 + q_{1,(n)} + \Delta\lambda h_1 = 0$$
$$b_2 = -q_2 + q_{2,(n)} + \Delta\lambda h_2 = 0$$
$$F = 0 \tag{A.1}$$

where

$$h_0 = 1 \tag{A.2}$$

Linearization of the above and $\Delta e^{p(k)} = -C_\approx^{e-1} : \Delta\sigma^{(k)}$ gives

$$a^{(k)} + C_\approx^{e-1} : \Delta\sigma^{(k)} + \Delta\lambda^{(k)}\Delta n^{(k)} + \delta\lambda^{(k)} n^{(k)} = 0$$
$$b_0^{(k)} - \Delta q_0^{(k)} + \delta\lambda^{(k)} = 0$$
$$b_1^{(k)} - \Delta q_1^{(k)} + \Delta\lambda^{(k)}\Delta h_1^{(k)} + \delta\lambda^{(k)} h_1^{(k)} = 0$$
$$b_2^{(k)} - \Delta q_2^{(k)} + \Delta\lambda^{(k)}\Delta h_2^{(k)} + \delta\lambda^{(k)} h_2^{(k)} = 0$$
$$F^{(k)} + \begin{bmatrix} \partial F_\sigma & \partial F_{qi} \end{bmatrix}\{\Delta\sigma^{(k)} \quad \Delta qi^{(k)}\}^T$$
$$= F^{(k)} + \partial F_\sigma : \Delta\sigma^{(k)} + \partial F_{q0} : \Delta q0^{(k)} + \partial F_{q1} : \Delta q1^{(k)} + \partial F_{q2} : \Delta q2^{(k)} = 0 \tag{A.3}$$

where

$$\Delta n^{(k)} = (\partial n_\sigma)^{(k)} : \Delta\sigma^{(k)} + (\partial n_{q1})^{(k)} : \Delta q_1^{(k)} + (\partial n_{q2})^{(k)} : \Delta q_2^{(k)}$$
$$\Delta h_0^{(k)} = 0$$
$$\Delta h_1^{(k)} = (\partial h1_\sigma)^{(k)} : \Delta\sigma^{(k)} + (\partial h1_{q1})^{(k)} : \Delta q1^{(k)} + (\partial h1_{q2})^{(k)} : \Delta q2^{(k)}$$
$$\Delta h_2^{(k)} = (\partial h2_\sigma)^{(k)} : \Delta\sigma^{(k)} + (\partial h2_{q1})^{(k)} : \Delta q1^{(k)} + (\partial h2_{q2})^{(k)} : \Delta q2^{(k)} \tag{A.4}$$

where $\partial h1_\sigma$ means first derivative of h_1 with respect to σ.

$$\partial h1_\sigma = C_1(f_p - n\overline{\sigma})/(f_p)^2$$
$$\partial h1_{q0} = 0$$
$$\partial h1_{q1} = -\partial h1_\sigma - \gamma$$
$$\partial h1_{q2} = -\partial h1_\sigma \tag{A.5}$$

and

$$\partial h2_\sigma = C\partial h1_\sigma$$
$$\partial h2_{q0} = 0$$
$$\partial h2_{q1} = -C\,\partial h1_\sigma$$
$$\partial h2_{q2} = -C\,\partial h1_\sigma \tag{A.6}$$

and

$$\partial F_\sigma = m$$
$$\partial F_{q0} = -H$$
$$\partial F_{q1} = -m$$
$$\partial F_{q2} = -m \tag{A.7}$$

and

$$\partial n_{q1} = \partial n_{q2} = -\partial n_\sigma$$
$$C = C_2/C_1 \tag{A.8}$$

The system of equations in (A.3) can be written in matrix form

$$[A^{(k)}]^{-1}\begin{Bmatrix} \Delta\sigma^{(k)} \\ \Delta q_0^{(k)} \\ \Delta q_1^{(k)} \\ \Delta q_2^{(k)} \end{Bmatrix} + \{\tilde{a}^{(k)}\} + \delta\lambda^{(k)}\{\tilde{r}^{(k)}\} = 0 \tag{A.9}$$

where

$$[A^{(k)}]^{-1} = \begin{bmatrix} C_\approx^{e-1} + \Delta\lambda^{(k)}.\partial n_\sigma^{(k)} & 0 & \Delta\lambda^{(k)}.\partial n_{q1}^{(k)} & \Delta\lambda^{(k)}.\partial n_{q2}^{(k)} \\ 0 & -1 & 0 & 0 \\ \Delta\lambda^{(k)}.(\partial h1_\sigma)^{(k)} & 0 & \Delta\lambda^{(k)}.(\partial h1_{q1})^{(k)}-1 & \Delta\lambda^{(k)}.(\partial h1_{q2})^{(k)} \\ \Delta\lambda^{(k)}.(\partial h2_\sigma)^{(k)} & 0 & \Delta\lambda^{(k)}.(\partial h2_{q1})^{(k)} & \Delta\lambda^{(k)}.(\partial h2_{q2})^{(k)}-1 \end{bmatrix} \tag{A.10}$$

$$\{\tilde{a}^{(k)}\} = \begin{Bmatrix} a^{(k)} \\ b_0^{(k)} \\ b_1^{(k)} \\ b_2^{(k)} \end{Bmatrix}, \quad \{\tilde{r}^{(k)}\} = \begin{Bmatrix} n^{(k)} \\ 1 \\ h_1^{(k)} \\ h_2^{(k)} \end{Bmatrix} \tag{A.11}$$

Because equivalent plastic strain ($q_0^{(k)}$) and compliance have a linear relation then

$$b_0^{(k)} = 0 \tag{A.12}$$

Therefore

$$\begin{Bmatrix} \Delta\sigma^{(k)} \\ \Delta q_0^{(k)} \\ \Delta q_1^{(k)} \\ \Delta q_2^{(k)} \end{Bmatrix} = -[A^{(k)}]\{\tilde{a}^{(k)}\} - \delta\lambda^{(k)}[A^{(k)}]\{\tilde{r}^{(k)}\} \tag{A.13}$$

Using (A.4)–(A.8) in (A.10) and determining the $[A^{(k)}]$

$$[A^{(k)}] = \begin{pmatrix} A_{\approx 11}^{(k)} & 0 & A_{\approx 13}^{(k)} & A_{\approx 14}^{(k)} \\ 0 & -1 & 0 & 0 \\ A_{\approx 31}^{(k)} & 0 & A_{\approx 33}^{(k)} & A_{\approx 34}^{(k)} \\ A_{\approx 41}^{(k)} & 0 & A_{\approx 43}^{(k)} & A_{\approx 44}^{(k)} \end{pmatrix} \tag{A.14}$$

where

$$A_{\approx 11}^{(k)} = X_\approx^{-1}(\beta_3^{(k)} + \beta_2^{(k)}(1 + C\beta_3^{(k)}))$$
$$A_{\approx 13}^{(k)} = -X_\approx^{-1}\beta_{\approx 1}^{(k)}$$
$$A_{\approx 14}^{(k)} = -X_\approx^{-1}\beta_{\approx 1}^{(k)}\beta_3^{(k)} \tag{A.15}$$

and

$$A_{\approx 31}^{(k)} = X_\approx^{-1}\beta_2^{(k)}$$
$$A_{\approx 33}^{(k)} = -X_\approx^{-1}(\beta_{\approx 1}^{(k)} + C_\approx^{e-1}(1 + C\beta_2^{(k)}))$$
$$A_{\approx 34}^{(k)} = X_\approx^{-1}C_\approx^{e-1}\beta_2^{(k)} \tag{A.16}$$

and

$$A_{\approx 41}^{(k)} = X_\approx^{-1}C\beta_2^{(k)}\beta_3^{(k)}$$
$$A_{\approx 43}^{(k)} = X_\approx^{-1}C_\approx^{e-1}C\beta_2^{(k)}$$
$$A_{\approx 44}^{(k)} = -X_\approx^{-1}(\beta_{\approx 1}^{(k)}\beta_3^{(k)} + C_\approx^{e-1}(\beta_2^{(k)} + \beta_3^{(k)})) \tag{A.17}$$

and

$$\beta_{\approx 1}^{(k)} = \Delta\lambda^{(k)}.(\partial n_\sigma)^{(k)}$$
$$\beta_2^{(k)} = \Delta\lambda^{(k)}.(\partial h1_\sigma)^{(k)}$$
$$\beta_3^{(k)} = \Delta\lambda^{(k)}.\gamma + 1 \tag{A.18}$$

and

$$\underset{\approx}{X}^{(k)} = \underset{\approx 1}{\beta}^{(k)} \beta_3^{(k)} + \underset{\approx}{C}^{e-1} \left(\beta_2^{(k)} + \beta_3^{(k)} + C\beta_2^{(k)}\beta_3^{(k)} \right) \tag{A.19}$$

Substituting (A.13) in the last part of (A.3)

$$\delta\lambda^{(k)} = \frac{F^{(k)} - \left[\partial F_\sigma \quad \partial F_{qi} \right] A^{(k)} \tilde{a}^{(k)}}{\left[\partial F_\sigma \quad \partial F_{qi} \right] A^{(k)} \tilde{r}^{(k)}}$$

$$= \frac{F^{(k)} - m : [A^{(k)}]_\sigma \tilde{a}^{(k)} + m : [A^{(k)}]_{q1}\tilde{a}^{(k)} + m : [A^{(k)}]_{q2}\tilde{a}^{(k)}}{H + m : [A^{(k)}]_\sigma \tilde{r}^{(k)} - m : [A^{(k)}]_{q1}\tilde{r}^{(k)} - m : [A^{(k)}]_{q2}\tilde{r}^{(k)}} \tag{A.20}$$

where $[A^{(k)}]_\sigma$ denotes the row of $A^{(k)}$ associated to σ (first, second, third and fourth row of $A^{(k)}$ respectively for σ, q_0, $\boldsymbol{q}_1$ and $\boldsymbol{q}_2$). Note that

$$H[A^{(k)}]_{q0}\tilde{a}^{(k)} = 0$$
$$-H[A^{(k)}]_{q0}\tilde{r}^{(k)} = H \tag{A.21}$$

when $\delta\lambda^{(k)}$ is determined, $\Delta\sigma^{(k)}$, $\Delta q_0^{(k)}$, $\Delta\boldsymbol{q}_1^{(k)}$ and $\Delta\boldsymbol{q}_2^{(k)}$ are updated using (A.3) and subsequently the internal parameters are updated as following:

$$\varepsilon^{\boldsymbol{p}(k+1)} = \varepsilon^{\boldsymbol{p}(k)} + \Delta\varepsilon^{\boldsymbol{p}(k)} = \varepsilon^{\boldsymbol{p}(k)} - \underset{\approx}{C}^{e-1} : \Delta\sigma^{(k)}$$
$$q_0^{(k+1)} = q_0^{(k)} + \Delta q_0^{(k)}$$
$$\boldsymbol{q}_1^{(k+1)} = \boldsymbol{q}_1^{(k)} + \Delta\boldsymbol{q}_1^{(k)}$$
$$\boldsymbol{q}_2^{(k+1)} = \boldsymbol{q}_2^{(k)} + \Delta\boldsymbol{q}_2^{(k)}$$
$$\Delta\lambda^{(k+1)} = \Delta\lambda^{(k)} + \delta\lambda^{(k)}$$
$$\sigma^{(k+1)} = \sigma^{(k)} + \Delta\sigma^{(k)} \tag{A.22}$$

The continuum (standard) elasto-plastic tangent operator relates the stress to total strain rates. However, according to the Belytschko [43] the continuum (standard) elasto-plastic tangent operator can generate spurious loading and unloading condition during the abrupt transition from elastic to plastic. In addition, the consistent (algorithmic) tangent modulus is required to preserve the quadratic rate of asymptotic convergences inherent in the Newton–Raphson's iteration nested in the fully implicit backward Euler algorithm [41]. Analogous to the previous approach for finding the rate variables at time step $n+1$, the consistent modulus is obtained by linearization of the constitutive equations to relate the stress increment to total strain increment at the time $t+1$. By following the same approach described in previous section but assuming the total strain as non-constant and residuals ($\{\tilde{a}^{(k)}\}$) as zero after many manipulations the closed form of consistent tangent modulus is obtained. It is noticed that non-symmetric consistent modulus converts to standard tangent operator by reducing the step size to zero. Furthermore both consistent and tangent moduli turn to elastic stiffness matrix when no plastic loading occurs.

We write the set of Eqs. (35a)–(35g) in rate form so that

$$d\sigma = \underset{\approx}{C}^e : (d\varepsilon - d\varepsilon^{\boldsymbol{p}})$$
$$d\varepsilon^{\boldsymbol{p}} = d(\Delta\lambda)\boldsymbol{n} + \Delta\lambda \, d\boldsymbol{n}$$
$$dq_0 = d(\Delta\lambda)$$
$$d\boldsymbol{q}_1 = d(\Delta\lambda)\boldsymbol{h}_1 + \Delta\lambda \, d\boldsymbol{h}_1$$
$$d\boldsymbol{q}_2 = d(\Delta\lambda)\boldsymbol{h}_2 + \Delta\lambda \, d\boldsymbol{h}_2$$
$$dF = \partial F_\sigma : d\sigma + \partial F_{q0} : dq_0 + \partial F_{q1} : d\boldsymbol{q}_1 + \partial F_{q2} : d\boldsymbol{q}_2 = 0 \tag{A.23}$$

where

$$d\boldsymbol{n} = \partial\boldsymbol{n}_\sigma : d\sigma + \partial\boldsymbol{n}_{q1} : d\boldsymbol{q}_1 + \partial\boldsymbol{n}_{q2} : d\boldsymbol{q}_2$$
$$d\boldsymbol{h}_0 = 0$$
$$d\boldsymbol{h}_1 = \partial\boldsymbol{h}_1/\partial\sigma : d\sigma + \partial\boldsymbol{h}_1/\partial\boldsymbol{q}_1 : d\boldsymbol{q}_1 + \partial\boldsymbol{h}_1/\partial\boldsymbol{q}_2 : d\boldsymbol{q}_2$$
$$d\boldsymbol{h}_2 = \partial\boldsymbol{h}_2/\partial\sigma : d\sigma + \partial\boldsymbol{h}_2/\partial\boldsymbol{q}_1 : d\boldsymbol{q}_1 + \partial\boldsymbol{h}_2/\partial\boldsymbol{q}_2 : d\boldsymbol{q}_2 \tag{A.24}$$

Substituting (A.23)_2 in (A.23)_1 and using (A.24) and solving for $d\sigma$ and $d\boldsymbol{q}$

$$\left\{ \begin{array}{c} d\sigma \\ dq_0 \\ d\boldsymbol{q}_1 \\ d\boldsymbol{q}_1 \end{array} \right\} = A\{\tilde{a}'\} - d(\Delta\lambda)A\{\tilde{r}\} \tag{A.25}$$

where

$$\{\tilde{a}'\} = \left\{ \begin{array}{c} d\varepsilon \\ 0 \\ 0 \\ 0 \end{array} \right\} \tag{A.26}$$

Substituting (A.25) into consistency condition (A.23)_6

$$d(\Delta\lambda) = \frac{\left[\partial F_\sigma \quad \partial F_{qi} \right] : A : \tilde{a}'}{\left[\partial F_\sigma \quad \partial F_{qi} \right] : A : \tilde{r}} \tag{A.27}$$

$$d(\Delta\lambda) = \frac{\boldsymbol{m} : [A]_\sigma \tilde{a}' - \boldsymbol{m} : [A]_{q1}\tilde{a}' - \boldsymbol{m} : [A]_{q2}\tilde{a}'}{\boldsymbol{m} : [A]_\sigma \tilde{r} + H - \boldsymbol{m} : [A]_{q1}\tilde{r} - m : [A]_{q2}\tilde{r}} \tag{A.28}$$

Substituting (A.29) into (A.25)

$$\left\{ \begin{array}{c} d\sigma \\ dq_0 \\ d\boldsymbol{q}_1 \\ d\boldsymbol{q}_2 \end{array} \right\} = \left[A - \frac{\left[\partial F_\sigma \quad \partial F_{qi} \right] : A}{\left[\partial F_\sigma \quad \partial F_{qi} \right] : A : \tilde{r}} A : \tilde{r} \right] : \left\{ \begin{array}{c} d\varepsilon \\ 0 \\ 0 \\ 0 \end{array} \right\} \tag{A.29}$$

Finally

$$\underset{\approx}{C}^{alg} = \underset{\approx 11}{A} - \frac{([A]\{\tilde{r}\}) \otimes \left(\left[\partial F_\sigma \quad \partial F_{qi} \right] : [A] \right)}{\left[\partial F_\sigma \quad \partial F_{qi} \right] : [A]\{\tilde{r}\}} \tag{A.30}$$

References

[1] Bridgman PW. The effect of hydrostatic pressure on the fracture of brittle substances. J Appl Phys 1947;18.
[2] Bridgman PW. Studies in large plastic flow and fracture with special emphasis on the effects of hydrostatic pressure. 1st ed. New York: McGraw-Hill; 1952.
[3] Khan AS, Huang S. Continuum theory of plasticity. New York: Wiley; 1995.
[4] Hill R. A Theory of the yielding and plastic flow of anisotropic metals. Proc R Soc London Ser A Math Phys Sci 1948;193:281–97.
[5] Barlat F, Brem JC, Yoon JW, Chung K, Dick RE, Lege DJ, et al. Plane stress yield function for aluminum alloy sheets – part 1: theory. Int J Plasticity 2003;19:1297–319.
[6] Barlat F, Maeda Y, Chung K, Yanagawa M, Brem JC, Hayashida Y, et al. Yield function development for aluminum alloy sheets. J Mech Phys Solids 1997;45:1727–63.
[7] Barlat F, Aretz H, Yoon JW, Karabin ME, Brem JC, Dick RE. Linear transfomation-based anisotropic yield functions. Int J Plasticity 2005;21:1009–39.
[8] Barlat F, Yoon JW, Cazacu O. On linear transformations of stress tensors for the description of plastic anisotropy. Int J Plasticity 2007;23:876–96.
[9] Banabic D, Aretz H, Comsa DS, Paraianu L. An improved analytical description of orthotropy in metallic sheets. Int J Plasticity 2005;21:493–512.
[10] Cazacu O, Barlat F. A new anisotropic yield criterion for aluminum alloys. Adv Mater Forum I 2002;230–2:537–40.
[11] Cazacu O, Barlat F. A criterion for description of anisotropy and yield differential effects in pressure-insensitive metals. Int J Plasticity 2004;20:2027–45.
[12] Cazacu O, Barlat F, Nixon ME. New anisotropic constitutive models for HCP sheet forming simulations. In: Ghosh S, Castro JM, Lee JK, editors. Materials processing and design: modeling, simulation and applications, Pts 1 and 2. Melville: Amer Inst Physics; 2004. p. 1046–51.
[13] Cazacu O, Plunkett B, Barlat F. Orthotropic yield criterion for hexagonal closed packed metals. Int J Plasticity 2006;22:1171–94.
[14] Hu W. Constitutive modeling of orthotropic sheet metals by presenting hardening-induced anisotropy. Int J Plasticity 2007;23:620–39.
[15] Bron F, Besson J. A yield function for anisotropic materials – application to aluminum alloys. Int J Plasticity 2004;20:937–63.
[16] Karafillis AP, Boyce MC. A general anisotropic yield criterion using bounds and a transformation weighting tensor. J Mech Phys Solids 1993;41:1859–86.

[17] Barlat F, Gracio JJ, Lee M-G, Rauch EF, Vincze G. An alternative to kinematic hardening in classical plasticity. Int J Plasticity 2011;27:1309–27.

[18] Stoughton TB. A non-associated flow rule for sheet metal forming. Int J Plasticity 2002;18:687–714.

[19] Spitzig WA, Richmond O. The effect of pressure on the flow-stress of metals. Acta Metall 1984;32:457–63.

[20] Stoughton TB, Yoon JW. Review of Drucker's postulate and the issue of plastic stability in metal forming. Int J Plasticity 2006;22:391–433.

[21] Lade P, Nelson R, Ito Y. Nonassociated flow and stability of granular materials. J Eng Mech 1987;113:1302–18.

[22] Yoon JW, Stoughton TB, Dick RE. Earing prediction in cup drawing based on non-associated flow rule. In: CeasarDeSa JMA, Santos AD, editors. NUMIFORM '07: materials processing and design: modeling, simulation and applications, Pts I and II. Melville: Amer Inst Physics; 2007. p. 685–90.

[23] Stoughton TB, Yoon JW. A pressure-sensitive yield criterion under a non-associated flow rule for sheet metal forming. Int J Plasticity 2004;20:705–31.

[24] Cvitanic V, Vlak F, Lozina Z. A finite element formulation based on non-associated plasticity for sheet metal forming. Int J Plasticity 2008;24:646–87.

[25] Stoughton TB, Yoon JW. Anisotropic hardening and non-associated flow in proportional loading of sheet metals. Int J Plasticity 2009;25:1777–817.

[26] Taherizadeh A, Green DE, Ghaei A, Yoon JW. A non-associated constitutive model with mixed iso-kinematic hardening for finite element simulation of sheet metal forming. Int J Plasticity 2010;26:288–309.

[27] Zang SL, Guo C, Thuillier S, Lee MG. A model of one-surface cyclic plasticity and its application to springback prediction. Int J Mech Sci 2011;53:425–35.

[28] Chaboche JL. Time-independent constitutive theories for cyclic plasticity. Int J Plasticity 1986;2:149–88.

[29] Yoon JW, Yang DY, Chung K. Elasto-plastic finite element method based on incremental deformation theory and continuum based shell elements for planar anisotropic sheet materials. Comput Method Appl M 1999;174:23–56.

[30] Yoon JW, Barlat F, Dick RE, Karabin ME. Prediction of six or eight ears in a drawn cup based on a new anisotropic yield function. Int J Plasticity 2006;22:174–93.

[31] Yoshida F, Uemori T. A model of large-strain cyclic plasticity describing the Bauschinger effect and workhardening stagnation. Int J Plasticity 2002;18:661–86.

[32] Armstrong, PJ, Frederick, CO, A mathematical representation of the multiaxial Bauschinger effect, Central Electricity Generating Board Report, Berkeley Nuclear Laboratories, RD/B/N 731; 1966.

[33] Ziegler H. A modification of Prager's hardening rule. Q Appl Mech 1959;17:55–65.

[34] Geng LM, Wagoner RH. Role of plastic anisotropy and its evolution on springback. Int J Mech Sci 2002;44:123–48.

[35] Yoshida F, Uemori T. A model of large-strain cyclic plasticity and its application to springback simulation. Int J Mech Sci 2003;45:1687–702.

[36] Lee MG, Kim D, Kim C, Wenner ML, Wagoner RH, Chung KS. A practical two-surface plasticity model and its application to spring-back prediction. Int J Plasticity 2007;23:1189–212.

[37] Chun BK, Jinn JT, Lee JK. Modeling the Bauschinger effect for sheet metals, part I: theory. Int J Plasticity 2002;18:571–95.

[38] Chun BK, Kim HY, Lee KJ. Modeling the Bauschinger effect for sheet metals, part II: applications. Int J Plasticity 2002;18:597–616.

[39] Chaboche JL. A review of some plasticity and viscoplasticity constitutive theories. Int J Plasticity 2008;24:1642–93.

[40] Swift HW. Plastic instability under plane stress. J Mech Phys Solids 1952;1:1–18.

[41] Simo JC, Hughes TJR. Computational inelasticity, interdisciplinary applied mathematics. New York: Springer; 1998.

[42] Wilkins, ML, Calculation of elastic-plastic flow. In: Other Information: Orig. Receipt Date: 31-DEC-64; 1963, p. Medium: X [Size: Pages: 63].

[43] Belytschko T, Liu WK, Moran B. Nonlinear finite elements for continua and structures. Chichester: John Wiley; 2000.

[44] Simo JC, Taylor RL. A return mapping algorithm for plane-stress elastoplasticity. Int. J. Numer. Methods Eng. 1986;22:649–70.

[45] Yoon JW, Dick RE, Barlat F. A new analytical theory for earing generated from anisotropic plasticity. Int J Plasticity 2011;27:1165–84.

[46] Lee M-G, Kim D, Kim C, Wenner ML, Wagoner RH, Chung K. Spring-back evaluation of automotive sheets based on isotropic-kinematic hardening laws and non-quadratic anisotropic yield functions: Part II: characterization of material properties. Int J Plasticity 2005;21:883–914.

[47] Chung K, Lee SY, Barlat F, Keum YT, Park JM. Finite element simulation of sheet forming based on a planar anisotropic strain-rate potential. Int J Plasticity 1996;12:93–115.

[48] Yoon JW, Barlat F, Chung K, Pourboghrat F, Yang DY. Earing predictions based on asymmetric nonquadratic yield function. Int J Plasticity 2000;16:1075–104.